UC Riverside
UC Riverside Electronic Theses and Dissertations

Title
Transport Studies of the Electronic Properties of Graphene on Hexagonal Boron Nitride

Permalink
https://escholarship.org/uc/item/02s9x1fk

Author
Wang, Peng

Publication Date
2015

Peer reviewed|Thesis/dissertation

eScholarship.org Powered by the California Digital Library
University of California

UNIVERSITY OF CALIFORNIA
RIVERSIDE

Transport Studies of the Electronic Properties of Graphene on Hexagonal Boron Nitride

A Dissertation submitted in partial satisfaction
of the requirements for the degree of

Doctor of Philosophy

in

Physics

by

Peng Wang

March 2015

Dissertation Committee:

Dr. Marc Bockrath , Chairperson
Dr. Shan-Wen Tsai
Dr. Nathaniel Gabor

Copyright by
Peng Wang
2015

The Dissertation of Peng Wang is approved:

Committee Chairperson

University of California, Riverside

Acknowledgments

This dissertation can never be complete without the help and support from many people. I sincerely thank all those who made this dissertation possible and my graduate study the best experience that I will cherish forever.

First and foremost, I would like to thank my adviser Professor Marc Bockrath, for his guidance and mentorship, kind and patience, and consistent support during my PhD study at UCR. Not only taught me his expertise in carbon science, he always encouraged me to think independently and gave me the freedom to experiment on any new ideas that came up. Without his continuous encourage and valuble advices, I can never conquer the obstacles and stressful situations.

I would like to acknowledge Professor Shan-Wen Tsai and Professor Nathaniel Gabor for taking their previous time to be my dissertation committee and their constructive advice.

I enjoyed working with and getting to know my colleagues and friends in Bockrath's lab, including Tengfei Miao, Bin Cheng, Oley Martynov, Juan Aguilera Servin, Yong Wu, Chang Pan, Yi Wu, Sean Nelson, Andrei Nosek, Rui Lv, Nan Zhang. Without your help and passion, many experiments would be impossible. I would also like to thank previous group member Brian Standley for his help on measurement setups and data acquisition software.

I would like to thank Professor Jeanie Lau and her students for sharing me with their fabrication techniques, not to mention short term loans of equipments and liquid helium. This includes Lei Jing, Wenzhang Bao, Hang Zhang, Jairo Velasco, Fenglin Wang, Yongjin Lee, Jhao Wun Huang.

Last, but not least, I would like to thank my parents for their unconditional and endless love to me. They are always standing behind me, supporting and educating me during every stage of my life, no matter how far they are away from me. I especially thank my wife Qian Cai. I cherish every day in my PhD studies with her accompany, understanding, encourage and love.

To my parents for all the support.

ABSTRACT OF THE DISSERTATION

Transport Studies of the Electronic Properties of Graphene on Hexagonal Boron Nitride

by

Peng Wang

Doctor of Philosophy, Graduate Program in Physics
University of California, Riverside, March 2015
Dr. Marc Bockrath , Chairperson

Graphene's planar structure and unique low energy spectrum make it an intriguing material to study its electronic properties. Recent progresses in stacking graphene (G) on high quality hexagonal boron nitride (hBN) greatly advanced the electronic performance of graphene devices, approaching the intrinsic properties of graphene. This thesis reports transport studies of graphene on hBN, including graphene/hBN moiré superlattice at small rotation angle and ballistic transport in short/wide encapsulated BN/G/BN structures.

Chapter 1 will introduce the basic properties of graphene, including the unique low energy electronic spectrum and the unconventional integer quantum Hall effect. The concept of Berry's phase and pseudospin winding number and their connection to the quantum Hall effect are also discussed. Chapter 2 reviews the properties of graphene on hBN, especially the long wavelength moiré superlattice at small rotation angle which modulates graphene's low energy spectrum. It also discusses the Hofstadter's butterfly and its realization in the graphene/hBN heterostructure.

Chapter 3 addresses some of the essential techniques used to fabricate graphene/hBN devices measured in this thesis, including the layer stacking techniques and fabrication of graphene field effect transistors.

Chapter 4 reports the measurements of Hofstadter's butterfly spectrum focusing at the large doping region where the Fermi level is above the secondary Dirac points generated by the moiré superlattice. At large electron doping, we observed a novel π phase shift in the magneto-oscillations. At large hole doping, inversion symmetry breaking generates a distinct hexagonal pattern.

Chapter 5 discusses measurements of short BN/G/BN cavities. The high quality BN/G/BN devices exhibit ballistic transport behavior - Fabry-Pérot oscillations. The effects of magnetic field on the system are also investigated, showing signatures of "pseudodiffussive" transport at the charge neutrality point for finite fields.

Contents

List of Figures **x**

1 Introduction **1**
1.1 Introduction to Graphene . . . 2
1.1.1 Lattice Structure of Graphene . . . 2
1.1.2 Dirac Fermions in Graphene . . . 5
1.2 Integer Quantum Hall Effect and Berry Phase in Graphene . . . 9
1.2.1 Quantum Hall Effect . . . 9
1.2.2 Integer Quantum Hall Effect in Graphene . . . 12
1.2.3 Berry's Phase in Graphene . . . 13

2 Graphene on Hexagonal Boron Nitride **17**
2.1 High Quality Electronic Transport of Graphene on Hexagonal Boron Nitride 18
2.2 Graphene/hBN Moiré Superlattice . . . 19
2.3 Hofstadter's Butterfly Spectrum in Graphene/hBN Superlattice . . . 23

3 Sample Preparation and Device Fabrication **27**
3.1 Sample Isolation and Identification . . . 27
3.2 Mechanical Transfer of Graphene and Other Layered Materials . . . 30
3.2.1 Resist Assisted Transfer of Graphene . . . 31
3.2.2 Resist Free Transfer Technique . . . 34
3.3 Fabrication Graphene Field Effect Transistors . . . 36
3.3.1 Fabrication of Graphene/hBN FETs . . . 37
3.3.2 Fabrication of Edge Contacts to Encapsulated Graphene . . . 41
3.4 Comparison of Electronic Qualities of Graphene Devices . . . 42

4 Topological Winding Number Change and Broken Inversion Symmetry in a Hofstadter's Butterfly **45**

5 Ballistic Transport in Short Graphene cavities **66**
5.1 Device Fabrication and Characteristics . . . 66
5.2 Fabry-Pérot Oscillations in BN/G/BN Cavities . . . 69
5.3 Magnetotransport of BN/G/BN Cavities . . . 73

6 Conclusion **79**

List of Figures

1.1 Lattice structure of graphene. 4
1.2 Band structure of graphene. 7
1.3 Hall effect. 10
1.4 Pseudospin winding number in electron systems. 15

2.1 Moiré superlattice and minibands of graphene on hBN. 20
2.2 Transport signature of moiré minibands. 21
2.3 Diophantine diagram. 24
2.4 Conductance of an aligned graphene/hBN device in the B-n plane. . . . 25

3.1 Optical image of single and few layer graphene on SiO_2/Si substrate. . . 29
3.2 AFM image single and few layer graphene. 30
3.3 Illustration of the transfer method. 31
3.4 SEM image of graphene on hBN. 33
3.5 Optical image of a BN/G/BN sandwich structure. 36
3.6 Flow chart of the fabrication procedure of graphene FETs. 38
3.7 Optical and SEM image of a graphene/hBN device. 39
3.8 Schematic of edge contacts to sandwiched graphene. 41
3.9 Comparison of mobilities of G/SiO_2, G/hBN and BN/G/BN devices. . . 43

4.1 hBN/G heterostructure device geometry and transport properties. . . . 49
4.2 Magnetotransport in a hBN/G heterostructure device. 51
4.3 Transition in Berry's phase and corresponding electron orbits. 53
4.4 Replica Dirac points and gaps in hole side. 57
S4.1 Data for sample G2. 60
S4.2 Vertical line traces for sample G2 and G1. 62
S4.3 Horizontal line traces for sample G2 and G1. 64
S4.4 Data for sample G3. 65

5.1 Low temperature transport characteristics of BN/G/BN device. 68
5.2 Scanning electron microscope (SEM) image of BN/G/BN cavities. . . . 69
5.3 Fabry-Pérot oscillations in BN/G/BN cavity. 70
5.4 Temperature dependence of the Fabry-Pérot oscillations in a 300nm cavity. 72
5.5 Magnetotransport in a 300nm BN/G/BN cavities. 74
5.6 Magnetotransport in a 200nm and a 100nm cavities. 76
5.7 Pseudodiffusive transport near the charge neutrality point. 78

Chapter 1

Introduction

Graphene is a two dimensional carbon allotrope - a single layer of graphite. Since its first isolation from bulk graphite about 10 years ago[1], graphene quickly became the "wonder material" that attracted tremendous research interest owing to its many extraordinary properties. It is only one atom thick yet the strongest material ever measured[2]. It conducts electricity[1] and heat[3] very efficiently and nearly transparent[4]. Besides these great properties, graphene also provides a rich platform for fundamental condensed matter physics research due to its linear dispersion[5] at low energy which mimics relativistic physics.

This thesis reports the studies of the electronic transport properties of graphene on hexagonal boron nitride (hBN). In chapter 2, a brief induction will be given to the properties of graphene on hBN previous studied specially the Hofstadter's butterfly spectrum in aligned graphene/hBN heterostructures[6–8]. Chapter 3 covers some of the essential techniques for preparing graphene samples and fabricating graphene field effect transistors (FETs).

In chapter 4, we report our studies on electronic transport properties of the aligned graphene/hBN superlattice at the large carrier density region. Quite interestingly, we observed a π phase change in the magnetoresistance oscillations which we interpret as an additional π shift of Berry's phase originating from the change of topological winding number from odd to even for electrons. At large hole doping inversion symmetry breaking generates a distinct hexagonal pattern in the longitudinal resistivity.

Chapter 5 focuses on ballistic transport in short BN/G/BN cavities. We demonstrate fabricating short and wide ballistic cavities in which the length of the device is as short as $\sim$100nm. Due to the high quality of the encapsulated BN/G/BN samples, electrons travel ballistically in a wide range of carrier densities. We observed the crossover from Fabry-Pérot oscillations to Shubnikov-de Hass oscillations under perpendicular magnetic fields related the three different length scales, namely the sample length L, the electron mean free path l and the cyclotron radius R_C. We also report possible evidence of magneto-pseudodiffusive transport near the charge neutrality point.

In the remaining of this chapter, I will review and introduce the basic properties of graphene including the band structures and quantum Hall effect. Special attention will be paid to the concept of Berry's phase and it's relation to the unconventional quantum Hall effect[9, 10], which strongly related to chapter 4.

1.1 Introduction to Graphene

1.1.1 Lattice Structure of Graphene

Graphene is a single atomic layer of carbon atoms in the form of a honeycomb structure (Figure 1.1a). Each carbon atoms has 6 electrons, which occupy the $1s^2$, $2s^2$ and $2p^2$ atomic orbitals. The $1s$ orbital is filled and thus strongly bonded. The $2s$,

$2p_x$, $2p_y$ and $2p_z$ (one $2s$ electron excited to p orbital) orbitals hybridize which leads to the formation of a σ band left with an extra p orbital in z direction. The σ band lies in the xy plane and fully filled which are responsible for the trigonal planar structure of graphene lattice. The remaining p orbital covalently bind with neighboring carbon atoms to form a π band.

The hexagonal lattice of graphene has two types non-equivalent carbon atoms also known as the A-B sublattices. Such lattice can be expressed as a triangular lattice with a basis of two atoms per unit cell. In Figure 1.1a, the A and B sublattices are shown in red and blue circles. Two possible unit cells are drawn as a rhombus and a hexagon in gray, each containing two carbon atoms. The primitive lattice vectors are drawn as red arrows in Figure 1.1b and can be written as:

$$\boldsymbol{a}_1 = a_0(\frac{\sqrt{3}}{2}, \frac{1}{2}), \;\; \boldsymbol{a}_2 = a_0(\frac{\sqrt{3}}{2}, -\frac{1}{2}), \tag{1.1}$$

where $a_0 \approx 2.46$Å is the lattice spacing. Correspondingly the primitive reciprocal lattice vectors are:

$$\boldsymbol{b}_1 = \frac{2\pi}{a_0}(\frac{1}{\sqrt{3}}, 1), \;\; \boldsymbol{b}_2 = \frac{2\pi}{a_0}(\frac{1}{\sqrt{3}}, -1). \tag{1.2}$$

The resulting reciprocal lattice is also a hexagonal lattice but rotated 90° with respect to the real space lattice, in which the K and K' points (Figure 1.1c) on the vertices of the hexagon are energy degenerate points. These points are also known as the Dirac point where the valence and conduction bands touch each other, which will become clear in the following section. The Γ point locates at the center of the Brillouin zone while the M point is in the middle point of an hexagon edge.

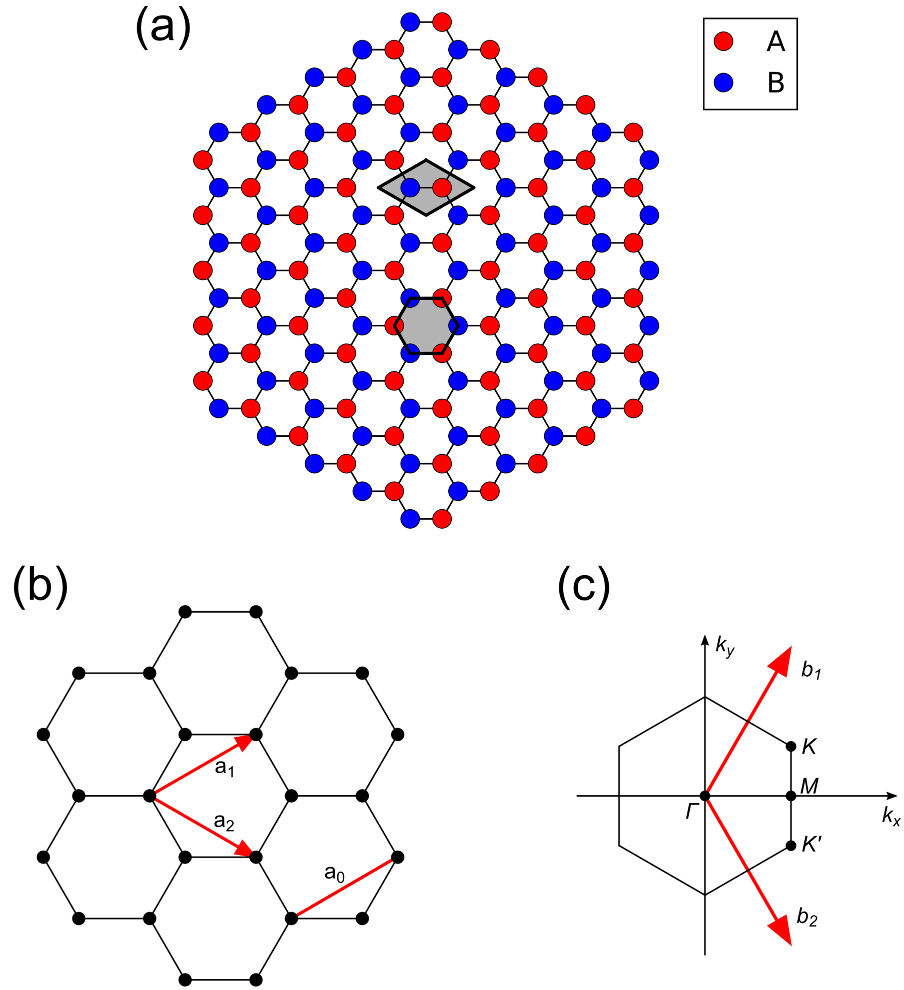

Figure 1.1: Honeycomb lattice of graphene and its Brillouin Zone. (a) Lattice structure of graphene with the red and blue circles representing the trigonal A and B sublattices respectively. The gray rhombus and hexagon are two example unit cells. (b) A zoomed in view of the lattice with primitive vectors drawn as red arrows ($\boldsymbol{a}_1$ and $\boldsymbol{a}_2$). (c) Corresponding Brillouin zone of the reciprocal lattice. The red arrows $\boldsymbol{b}_1$ and $\boldsymbol{b}_2$ are the primitive reciprocal lattice vectors. The Γ, M and K are highly symmetric points.

1.1.2 Dirac Fermions in Graphene

One of graphene's most unique properties is its linear dispersion spectrum near the K or K' points[5]. Considering the crystal Schrödinger equation problem:

$$H\psi = E(\boldsymbol{k})\psi. \tag{1.3}$$

Within the tight binding method following Wallace[5] and Neto[11], the Bloch wave function can be written as:

$$\psi = a\phi_1 + b\phi_2, \tag{1.4}$$

where

$$\phi_1 = \sum_A \phi(\boldsymbol{r} - \boldsymbol{R}_A)\ e^{i\boldsymbol{k}\cdot\boldsymbol{R}_A},\ \phi_2 = \sum_B \phi(\boldsymbol{r} - \boldsymbol{R}_B)\ e^{i\boldsymbol{k}\cdot\boldsymbol{R}_B}, \tag{1.5}$$

representing wave functions of A and B sublattices, linear combination of every carbon atoms' p_z orbital wave function $\phi(\boldsymbol{r})$. Integrating $\int d\boldsymbol{r}\phi_{1,2}^* H\psi = \int d\boldsymbol{r}\phi_{1,2}^* E\psi$ and ignoring overlap integrals $\int d\boldsymbol{r}\phi_{1,2}^*\phi_{2,1}$, we obtain

$$aH_{11} + bH_{12} = aNE, \tag{1.6}$$

$$aH_{21} + bH_{22} = bNE, \tag{1.7}$$

where

$$H_{11} = H_{22} = \int d\boldsymbol{r}\phi_1^* H\phi_1, \tag{1.8}$$

$$H_{12} = H_{21}^* = \int d\boldsymbol{r}\phi_1^* H\phi_2, \tag{1.9}$$

and N is the number of unit cells in the lattice, following from:

$$\begin{aligned}
\int d\boldsymbol{r}\phi_1^*\phi_1 &= \int d\boldsymbol{r}\phi_2^*\phi_2 \\
&= \sum_A \sum_{A'} e^{i\boldsymbol{k}\cdot(\boldsymbol{R}'_A - \boldsymbol{R}_A)} \int d\boldsymbol{r}\phi(\boldsymbol{r}-\boldsymbol{R}_A)^* \ \phi(\boldsymbol{r}-\boldsymbol{R}'_A) \\
&\approx \sum_A \sum_{A'} e^{i\boldsymbol{k}\cdot(\boldsymbol{R}'_A - \boldsymbol{R}_A)} \ \delta_{AA'} \\
&= \sum_A 1 = N.
\end{aligned} \tag{1.10}$$

In solving Equation 1.6 and 1.7, in order to have nonzero a and b value, we must have

$$\begin{vmatrix} H_{11} - NE & H_{12} \\ H_{12}^* & H_{22} - NE \end{vmatrix} = 0, \tag{1.11}$$

which gives the energy

$$E(\boldsymbol{k}) = \frac{H_{11}}{N} \pm \frac{|H_{12}|}{N}. \tag{1.12}$$

We then try to calculate H_{11} and H_{12}, notice that $H\phi = E_0\phi$, where E_0 is the carbon atomic energy of the p_z orbital

$$H_{11} = \int d\boldsymbol{r}\phi_1^* H\phi_1 \ = E_0 \int d\boldsymbol{r}\phi_1^*\phi_1 \ \approx NE_0. \tag{1.13}$$

For the H_{12} term

$$\begin{aligned}
H_{12} &= \int d\boldsymbol{r}\phi_1^* H\phi_2 \\
&= \sum_A \sum_B e^{i\boldsymbol{k}\cdot(\boldsymbol{R}_A - \boldsymbol{R}_B)} \int d\boldsymbol{r}\phi(\boldsymbol{r}-\boldsymbol{R}_A)^* \ \phi(\boldsymbol{r}-\boldsymbol{R}_B),
\end{aligned} \tag{1.14}$$

considering only the nearest neighbor hopping, the sum reduces to $\sum_A \sum_{n.n.}$,

$$\begin{aligned}
H_{12} &\approx \sum_A \sum_{n.n.} e^{i\boldsymbol{k}\cdot\boldsymbol{d}} \int d\boldsymbol{r}\phi^*(\boldsymbol{r}+\boldsymbol{d}) \ H\phi(\boldsymbol{r}) \\
&= -N\gamma_0 \sum_{n.n.} e^{i\boldsymbol{k}\cdot\boldsymbol{d}} \qquad . \\
&= -N\gamma_0(\ e^{i\boldsymbol{k}\cdot\boldsymbol{d}_1} + \ e^{i\boldsymbol{k}\cdot\boldsymbol{d}_2} + \ e^{i\boldsymbol{k}\cdot\boldsymbol{d}_3})
\end{aligned} \tag{1.15}$$

Where $\gamma_0 = \int d\boldsymbol{r}\phi^*(\boldsymbol{r}+\boldsymbol{d})H\phi(\boldsymbol{r}) \approx 2.8$eV[11] is the nearest neighbor hopping energy and $\boldsymbol{d}_{1,2,3}$ are the vectors pointing from a A atom to its nearest neighbor B atoms:

$$\boldsymbol{d}_1 = \frac{a_0}{\sqrt{3}}(\frac{1}{2}, \frac{\sqrt{3}}{2}),\ \boldsymbol{d}_1 = \frac{a_0}{\sqrt{3}}(-1, 0),\ \boldsymbol{d}_1 = \frac{a_0}{\sqrt{3}}(\frac{1}{2}, -\frac{\sqrt{3}}{2}). \tag{1.16}$$

Substituting the above results into Equation 1.12 and set $E_0 = 0$, we get:

$$E(\boldsymbol{k}) = \pm\gamma_0\sqrt{1 +\ 4\cos^2(\frac{a_0 k_y}{2}) +\ 4\cos(\frac{\sqrt{3}a_0 k_x}{2})\cos(\frac{a_0 k_y}{2})}. \tag{1.17}$$

The energy band structure is plotted in Figure 1.2. Coincidently, when the wave vector is at the corner of Brillouin Zone (K or K' points in Figure 1.1c)

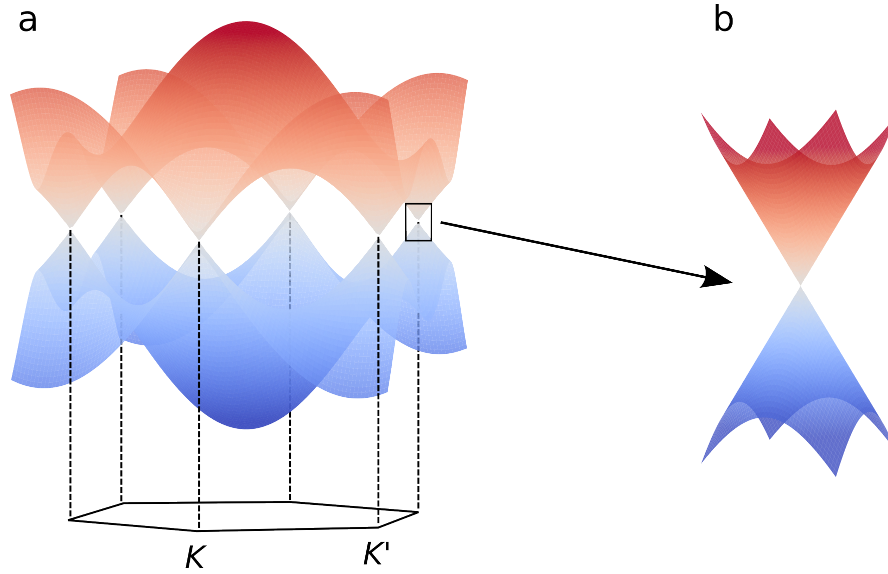

Figure 1.2: Band Structure of graphene

$$\boldsymbol{K} = \frac{4\pi}{3a_0}(\frac{\sqrt{3}}{2}, \frac{1}{2}),\ \boldsymbol{K'} = \frac{4\pi}{3a_0}(\frac{\sqrt{3}}{2}, -\frac{1}{2}), \tag{1.18}$$

the valence (π) and conduction (π^*) bands touch at zero energy. Zoom in to these points (Figure 1.2b), the energy dispersion is linearly dependent on wave vector $\boldsymbol{k}$. In the following discussion, we focus on the region close to a K point while similar results should apply to K' point. We can write the Taylor expansion of the energy in terms of

$\boldsymbol{q} = \boldsymbol{k} - \boldsymbol{K}$, where$|\boldsymbol{q}| \ll |\boldsymbol{K}|$:

$$E(\boldsymbol{q}) = \pm \hbar v_F |\boldsymbol{q}| + O[(q/K)^2], \tag{1.19}$$

the leading term is linear in $|\boldsymbol{q}|$ with a constant Fermi velocity $v_F = \frac{\sqrt{3}}{2}\gamma_0 a_0/\hbar \approx 1 \times 10^6 \mathrm{m/s}$. One direct consequence of the linear dispersion is that electrons behave like relativistic particles which are the so-called Dirac fermions. The effective Hamiltonian around a K point is $H = \hbar v_F \boldsymbol{\sigma} \cdot \boldsymbol{k}$, where $\boldsymbol{\sigma} = (\sigma_x, \sigma_y)$ are the Pauli matrices. So the electron wave function satisfies the two dimensional Dirac equation

$$\boldsymbol{\sigma} \cdot \boldsymbol{k} \psi = \pm |\boldsymbol{k}| \psi. \tag{1.20}$$

In momentum space, it is in the form of

$$\psi_{\pm, \boldsymbol{K}}(\boldsymbol{k}, \boldsymbol{r}) = \frac{1}{\sqrt{2}} \begin{pmatrix} 1 \\ \pm e^{i\theta_{\boldsymbol{k}}} \end{pmatrix} e^{i\boldsymbol{k}\cdot\boldsymbol{r}}, \tag{1.21}$$

where $\theta_{\boldsymbol{k}} = \arctan k_y/k_x$. The $\pm$ represents the electron (+) and hole band (-). This two component wave function originated from the two sublattices of carbon atoms A and B adding an extra degree of freedom-pseudospin to the electron states in graphene. We note that in Equation 1.20, ψ can be thought of as the eigenstate of spinor operator $\boldsymbol{\sigma}$ projected along the momentum operator $\boldsymbol{k}$ and has eigenvalues of (pseudo)spin up (+) or down (-) for the electron or hole bands. This suggests the states above and below the Dirac points have opposite chirality. In other words, the pseudospin has the same direction as $\boldsymbol{k}$ for electron states and opposite direction as $\boldsymbol{k}$ for hole states. The concept of pseudospin and chirality is of fundamental importance in the understanding of many interesting physical phenomena such as Klein tunneling[12–15] and integer quantum Hall effect[9, 10, 16] in graphene.

1.2 Integer Quantum Hall Effect and Berry Phase in Graphene

1.2.1 Quantum Hall Effect

The conventional Hall effect is observed when a two dimensional electrical current is subject to a perpendicular magnetic field (B), first reported by Hall[17]. It arises from the fact that electrons are deflected by the Lorentz force and accumulate on the two edges of the conducting channel, creating a transverse electric field until it cancels the Lorentz force. As shown in Figure 1.3a, a uniform current flows in the x-direction and is subject to magnetic field, we then define the longitudinal (ρ_{xx}) and Hall (ρ_{xy}) resistivity as:

$$\rho_{xx} = \frac{V_{xx}}{I}\frac{W}{L}, \ \rho_{xy} = \frac{V_{xy}}{I}. \tag{1.22}$$

Correspondently, the conductivities are:

$$\sigma_{xx} = \frac{\rho_{xx}}{\rho_{xx}^2 + \rho_{xy}^2}, \ \sigma_{xy} = \frac{\rho_{xy}}{\rho_{xx}^2 + \rho_{xy}^2}. \tag{1.23}$$

The Hall effect was well understood with the classical Drude model until the discovery of the integer quantum Hall effect by Klaus von Klitzing when studying the 2D Si MOSFET samples in 1980[18]. The observed Hall conductivity exhibits quantized values at low temperature and high magnetic field while longitudinal conductivity vanishes,

$$\sigma_{xx} = 0, \sigma_{xy} = \nu\frac{e^2}{h}, \tag{1.24}$$

where e is the electron charge, h is the Plank's constant and ν is an integer.

Integer quantum Hall effect is a direct result of quantum mechanics on the macroscopic scales. This phenomenon arises from the quantization of electron cyclotron orbits and Landau levels (LLs) under a perpendicular magnetic field. A single and continuous electron band is split into a set of discrete while highly degenerate levels

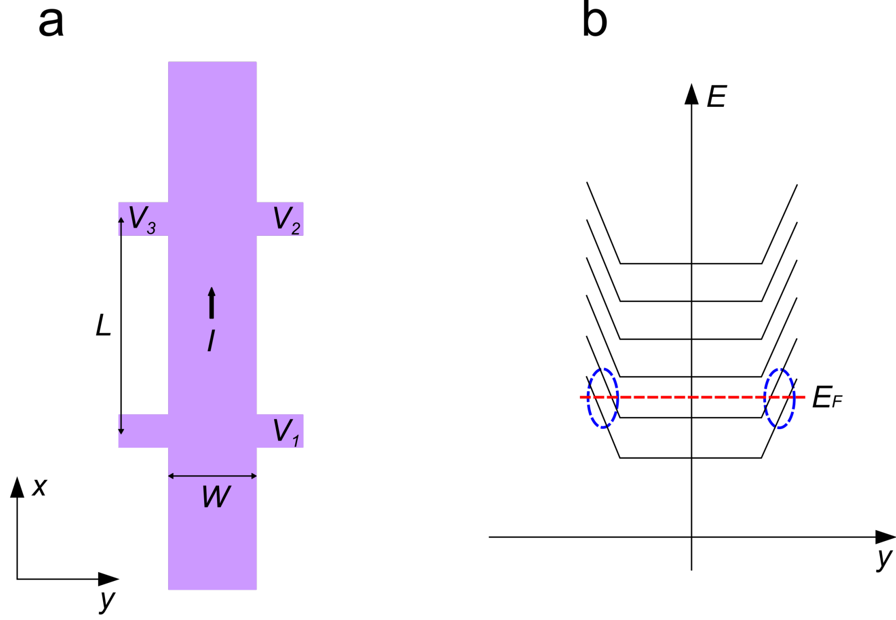

Figure 1.3: Hall effect. (a) Hall measurement setup. A uniform current I is following in x direction. The sample length and width are L and W respectively. $V_{xx} = V_1 - V_2$ is the longitudinal voltage and $V_{xy} = V_2 - V_3$ is the Hall voltage. A perpendicular magnetic field B is applied to the sample in the direction pointing out of the page. (b) Landau levels. Each black curve represents a Landau level where the spectrum is bended close to the edge of the sample giving rise to a 1D conducting channel. The red dashed line indicates the position of Fermi energy E_F.

given by $E_n = \hbar\omega_C(n + \frac{1}{2})$ and $\omega_C = \frac{eB}{m_e c}$ is the cyclotron frequency, resulting in a sequence of δ-peaks in the density of states (DOS)[19]:

$$\rho(E) = \sum_n g_n \delta(E - E_n), \tag{1.25}$$

where g_n accounts for the degeneracy of energy levels. When the electron Fermi energy (E_F) is fixed, varying the B field will change the energy separation of LLs and therefore the δ-peaks in the Equation 1.25 will sequentially cross E_F leading to a set of conductance peaks. In real samples, the δ-peaks are broadened due to scattering or thermal fluctuations and merged into an oscillating function in energy. Thus the observed

conductance is not δ-peaks but instead becomes maximal when E_F lies on a LL and minimal when E_F is in between of two LLs. This phenomenon is called Shubnikov-de Hass oscillation (SdHO) and was observed long before the discovery of QHE when the B field is small but sufficiently large. In order to observe the SdHO, it requires the B field to be strong enough so that electrons can finish at least one cyclotron orbit without being scattered.

As the magnetic field continues to increase, the LLs are further separated and eventually there exists energy ranges where DOS is zero. Then, either changing E_F or B will lead to vanishing longitudinal conductivity when E_F lies in the energy range of zero DOS, and constant plateau value of Hall conductivity. The width in energy of the plateau is the same as that of zero DOS, which also implies that the broadening of LLs is essential for the observation of QHE because otherwise the width of plateaus will be too small to resolve. To understand the plateau values of Hall conductivity, the Schrödinger equation of electron motion in a rectangular (Figure 1.3a) sample is solved using a Landau gauge[19], the resulting energy spectrum is:

$$E_n = \hbar\omega_C \left(n + \frac{1}{2}\right) + V(y). \tag{1.26}$$

The term $V(y)$ comes from the confinement of the boundary conditions and is independent of x, which readily means each edge of the sample is equipotential forming 1D conducting channels. As drawn in Figure 1.3b, the LLs are bended close to the edges of the sample. As a result, the number of conducting channels at a certain E_F in between two LLs is exactly the number of filled LLs (filling factor ν) each contributes one conductance quanta $G_0 = e^2/h$ in agreement with Equation 1.24. At the transition region (near a LL), the localized states contribute to the conductance which explains the steps between the quantized Hall plateaus.

Besides the integer quantum Hall effect, Hall plateaus have exhibited fractional values known as fractional quantum Hall effect (FQHE) and has different origins. Due to the scope of this thesis, it will not be discussed here.

1.2.2 Integer Quantum Hall Effect in Graphene

The quantum Hall effect in mono-layer and bilayer graphene[1, 9, 10] were immediately observed after the first isolation of graphene[1]. In summary, the observed quantized Hall conductivities exhibit values of $\pm(4n+2)\frac{e^2}{h}$ and $\pm(4n+4)\frac{e^2}{h}$ for mono-layer and bilayer graphene respectively, where n is an non-negative integer. Quite strikingly, there are no zero conductance plateaus in both cases as opposed to conventional two dimensional electron gas (2DEG). These unusual behavior can be seen from the Landau level spectrum of graphene[11, 20]

$$E_N = \mathrm{sgn}(N)\sqrt{2e\hbar B|N|}, \tag{1.27}$$

and bilayer graphene[16]

$$E_N = \mathrm{sgn}(N)\hbar\omega_C\sqrt{|N(N-1)|},\ \omega_C = eB/mc, \tag{1.28}$$

in the above equations the effective mass of bilayer graphene is $m \approx 0.054m_e$ and N is the LLs index. In both cases, there is a zero energy LL shared by both electron and hole states, responsible for the missing of zero Hall conductance plateau. The steps of $4\frac{e^2}{h}$ in σ_{xy} can be attributed to the electron spin and valley (pseudospin) degrees of freedom, each being two fold degenerate. Differently in the case of bilayer graphene, since N being 0 or 1 both result in a zero energy it adds an extra double degeneracy to the zero energy LL which gives rise to the step of $8\frac{e^2}{h}$ in σ_{xy} near the charge neutrality point (CNP).

The shift of the Hall plateau in graphene and graphene bilayer can be further understood by investigating the concept of Berry phase or pseudospin winding number which are the topics of the next section.

1.2.3 Berry's Phase in Graphene

Berry's Phase is defined as the geometric phase factor acquired as the eigenstate of a quantum system adiabatically varies its parameters along a closed path[21, 22]. In general, this phase can be written as:

$$\theta = \oint_C d\boldsymbol{R} \cdot A_n(\boldsymbol{R}), \tag{1.29}$$

where $A_n(\boldsymbol{R}) = i \langle n(\boldsymbol{R})| \nabla_{\boldsymbol{R}} |n(\boldsymbol{R})\rangle$ is called the Berry connection. The integral is over a closed path C in the parameter space $\boldsymbol{R}$ and $\boldsymbol{R}(t)$ varies in time.

In connection to the quantum Hall effect, only the topological Berry's phase arising from the spinor part of the wavefunction is relevant[16, 23, 24]. In the context of graphene, it is the phase that the electron wave function acquires as $\boldsymbol{k}$ evolves adiabatically along a closed path on the Fermi surface. Such an adiabatic process can be achieved by applying a perpendicular magnetic field to the 2D graphene plane so that the wave vector $\boldsymbol{k}$ rotates along a closed circle of constant energy on the Fermi surface. In connection to the quantum Hall effect, only the topological Berry's phase is relevant[16, 23–25] and can be obtained by evaluating the integral in Equation 1.29 using the spinor part of the wavefunction:

$$\begin{aligned} \theta &= -i \oint_C d\boldsymbol{k} \langle \psi(\boldsymbol{k})| \ \nabla_{\boldsymbol{k}} |\psi(\boldsymbol{k})\rangle \\ &= -i \oint_C d\boldsymbol{k} \ \frac{1}{2}(1, \pm e^{-i\theta_{\boldsymbol{k}}}) \begin{pmatrix} 0 \\ \pm i e^{i\theta_{\boldsymbol{k}}} \nabla_{\boldsymbol{k}} \theta_{\boldsymbol{k}} \end{pmatrix} = \pi. \end{aligned} \tag{1.30}$$

Similarly, we can perform the same calculation for bilayer graphene using its spinor electron wave function[16, 24, 25]

$$\psi_{\pm,\boldsymbol{K}} = \frac{1}{\sqrt{2}} \begin{pmatrix} 1 \\ \pm e^{2i\theta_{\boldsymbol{k}}} \end{pmatrix}, \tag{1.31}$$

which gives the Berry's phase $\theta = 2\pi$. Experimentally, this adiabatic process can be achieved by applying a perpendicular magnetic field to the 2D graphene plane so that the wave vector $\boldsymbol{k}$ rotates along a closed circle of constant energy on the Fermi surface.

The nontrivial Berry phase of π and 2π are responsible for the observed unconventional quantum Hall effect for mono and bilayer graphene[9, 10]. Later, Marzari[24] pointed out that the concept of topological pseudospin winding number w associated with the Berry's phase can be used to describe the quantum Hall effect in graphene and graphene bilayer. The pseudospin winding number describes how fast the pseudospin in the Dirac quasiparticles evolves as the wave vector rotates when $\boldsymbol{k}$ undergoes a closed path. It is the same quantity as "the degree of chirality" J[16, 26], which is 1 and 2 for mono and bilayer graphene. As a comparison, conventional 2DEG has no chiral degree of freedom and therefore $w = 0$. Figure 1.4[24] is an schematic illustration of the pseudospin distribution for three different systems. As we can see, the pseudospin in graphene rotates as fast as $\boldsymbol{k}$ while twice as fast as $\boldsymbol{k}$ in bilayer graphene; for a non-chiral 2DEG, there is no pseudospin.

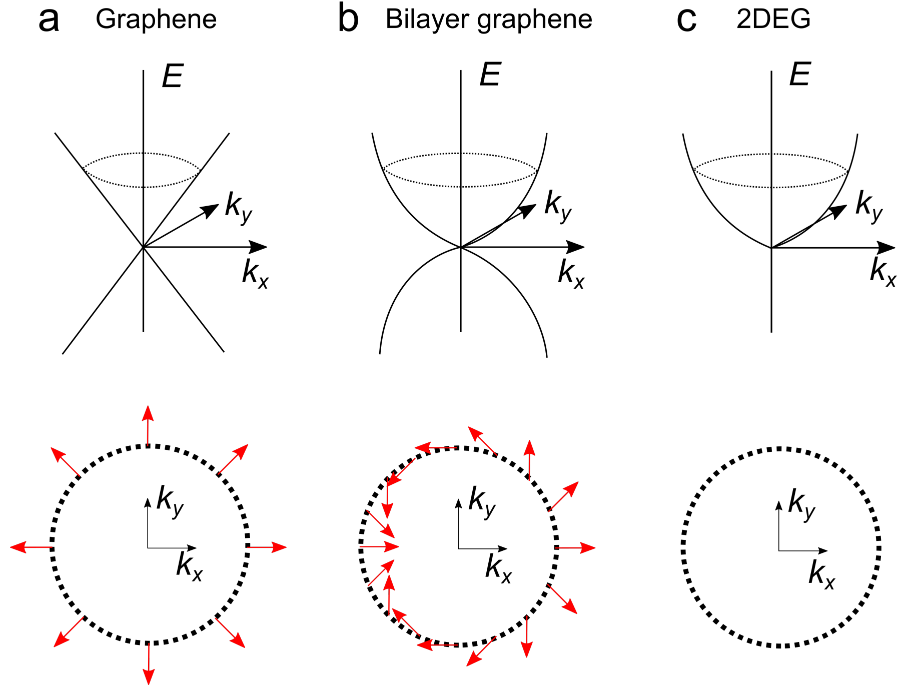

Figure 1.4: Illustration of pseudospin for low energy electrons. This figure is from Ref.[24] with modifications. (a) Upper panel: Energy dispersions for low energy electrons in graphene. Lower panel: Pseudospin distribution for eigenstates in graphene on an equi-energy contour specified by the dashed curve in upper panel. The red arrows represent the direction of pseudospin. Here, we consider the electronic states with wave vectors near the Dirac point K. (b) and (c) Similar quantities as in (a) for bilayer graphene and a conventional 2DEG, respectively.

More generally, the pseudospin winding number w equals the number of layers in graphene for ABC stacked layers at low energy. Therefore the effective Hamiltonian and wave function (spinor part) near the K point of n layers graphene with ABC stacking

can be rewritten in the following general form[16, 24, 27]:

$$H^n(\boldsymbol{k}) \propto k^w \begin{pmatrix} 0 & e^{-iw\theta_{\boldsymbol{k}}} \\ e^{iw\theta_{\boldsymbol{k}}} & 0 \end{pmatrix}, \tag{1.32}$$

$$\psi^n_{\pm,\boldsymbol{K}}(\boldsymbol{k}) = \frac{1}{\sqrt{2}} \begin{pmatrix} 1 \\ \pm e^{iw\theta_{\boldsymbol{k}}} \end{pmatrix}. \tag{1.33}$$

Besides the integer sequence of the quantum Hall plateaus, w also modulates the phase of magnetoresistance oscillations[10, 28, 29] determined by the semiclassical Bohr-Sommerfeld quantization condition:

$$\Delta\rho_{xx} = \rho(B,T)\cos\left[(2\pi(B_F/B + 1/2 + \beta)\right], \tag{1.34}$$

where B_F is the inverse of the period of the oscillations in $1/B$, $\rho(B,T)$ is the oscillation amplitude and $\beta = w/2$. This result will be used to determine w in our experiments on G/hBN superlattice in chapter 4.

Chapter 2

Graphene on Hexagonal Boron Nitride

In this chapter, I will introduce the background of graphene's electronic properties on hexagonal boron nitride (hBN). First, I will review previous studies on the electronic performance improvement when changing from SiO_2 to hBN substrates. Then, I will show our experimental observations on the transport properties of crystallographically aligned graphene/hBN superlattice, including secondary Dirac points (sDP) arising from the moiré minibands and Hofstadter's butterfly spectrum in magnetic field.

Isolated atomically thin graphene was first discovered on SiO_2 substrates by Novoselov et al.[1]. The small but visible optical contrast of graphene on SiO_2 makes it the perfect substrate for researchers to quickly enter the field[30]. However graphene/SiO_2 devices usually suffer from strong external perturbations limiting its electronic quality. Since 2008, suspending graphene by removing substrates brought graphene device quality to the next era approaching ballistic transport[31, 32]. However the suspended structures are mechanically fragile compared to those on substrates and lack the flex-

ibility of device architecture. Moreover, the fabrication processes for producing such devices is much more complicated. Therefore, it is highly desirable to have alternative substrates that can support graphene layers while retaining the high performance of suspended graphene.

2.1 High Quality Electronic Transport of Graphene on Hexagonal Boron Nitride

Previous studies revealed that the main scattering mechanisms limiting graphene/SiO_2 device performance come from charged impurities/inhomogeneity[33–36], surface roughness[37–39] and optical phonons of SiO_2[36, 40].

Single crystal hexagonal boron nitride (hBN) on the other hand is atomically flat and the surface roughness is significantly smaller[41, 42]. Scanning tunneling microscopy (STM) studies of graphene on both SiO_2 and hBN substrates[42] directly showed a much lower concentration of charge inhomogeneity ($\sim 10^9 cm^{-2}$ on hBN compared to $\sim 10^{11} cm^{-2}$ on SiO_2). In addition, hBN similar to graphene is a layered compound with the carbon atoms replaced by boron and nitrogen atoms on the two inequivalent sublattices. Due to the large onsite energy difference between boron and nitrogen atoms, hBN is an insulator with a band gap of 5.9eV[43] and a breakdown electric field of $\sim$0.7V/nm[41], making it a perfect dielectric for graphene electronics. Typical carrier mobilities of graphene on hBN devices are substantially larger than those of graphene on SiO_2 (a quantitative comparison of mobility will be made in chapter 3).

2.2 Graphene/hBN Moiré Superlattice

In addition to the improvement of electronic performance, the hBN lattice acts as a long wavelength electrostatic potential modulation to the electron states in graphene, forming moiré pattern[42, 44]. The resulting superlattice modifies graphene's low energy (near the Dirac point) electronic spectrum[45–47], generating minibands near the Brillouin zone (sBZ) edge of the superlattice and is predicted to induce a sizeable band gap[48].

A visual illustration of the graphene/hBN moiré superlattice is drawn in Fig. 2.1a with the red, blue and black solid circles corresponding to boron, nitrogen and carbon atoms respectively. An example superlattice unit cell is outlined in a yellow shadowed hexagon. Figure 2.1b plots an example of the low energy band structure near the main Dirac point of graphene, moiré minibands (green) are generated near the edge of the sBZ edge. The exact miniband structure will depend on the substrate parameters[47, 49].

Depending on the relative rotation angle θ between graphene and hBN lattices, the moiré wavelength is given by[44]

$$\lambda = \frac{(1+\delta)a_0}{\sqrt{2(1+\delta)\ (1-\cos\theta+\delta^2}}, \tag{2.1}$$

where $a_0 = 0.246$nm is the graphene lattice constant and $\delta = 1.8\%$ is the lattice mismatch between graphene and hBN. The dependence of the wavelength as a function of rotation angle is plotted in Fig. 2.1c, which reaches its maximum value of $\sim$14nm when the orientation of the two lattices are exactly aligned and quickly drops as θ increases.

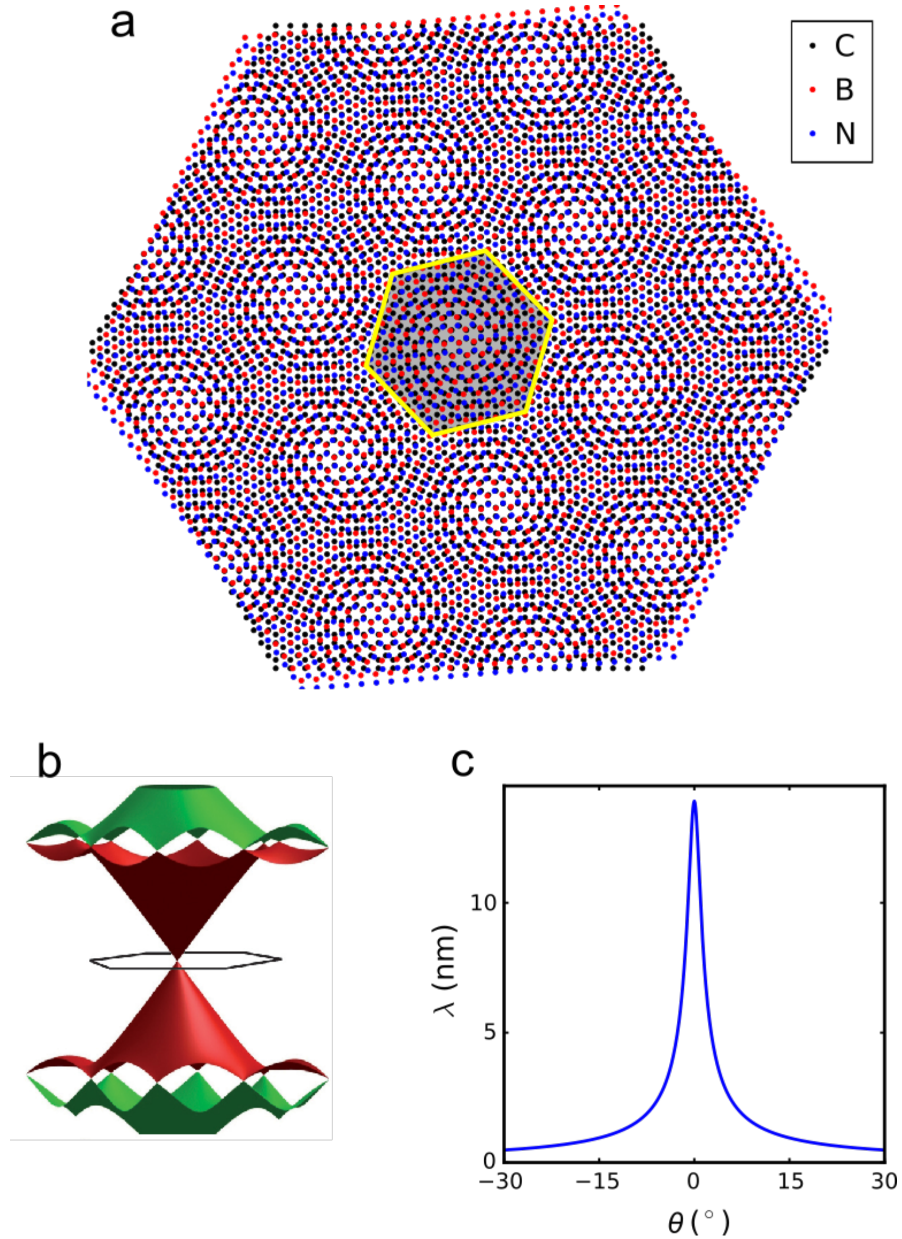

Figure 2.1: (a) Schematic diagram of the graphene/hBN moiré superlattice with a relative rotation angle of $\theta = 5°$. Red, blue and black solid circles represent boron, nitrogen and carbon atoms respectively. The yellow shadowed hexagon outlines a unit cell of the superlattice. (b) An example low energy band structure near the main Dirac point of graphene. This figure was taken from Ref.[49]. (c) Superlattice wavelength (λ) vs. rotation angle (θ).

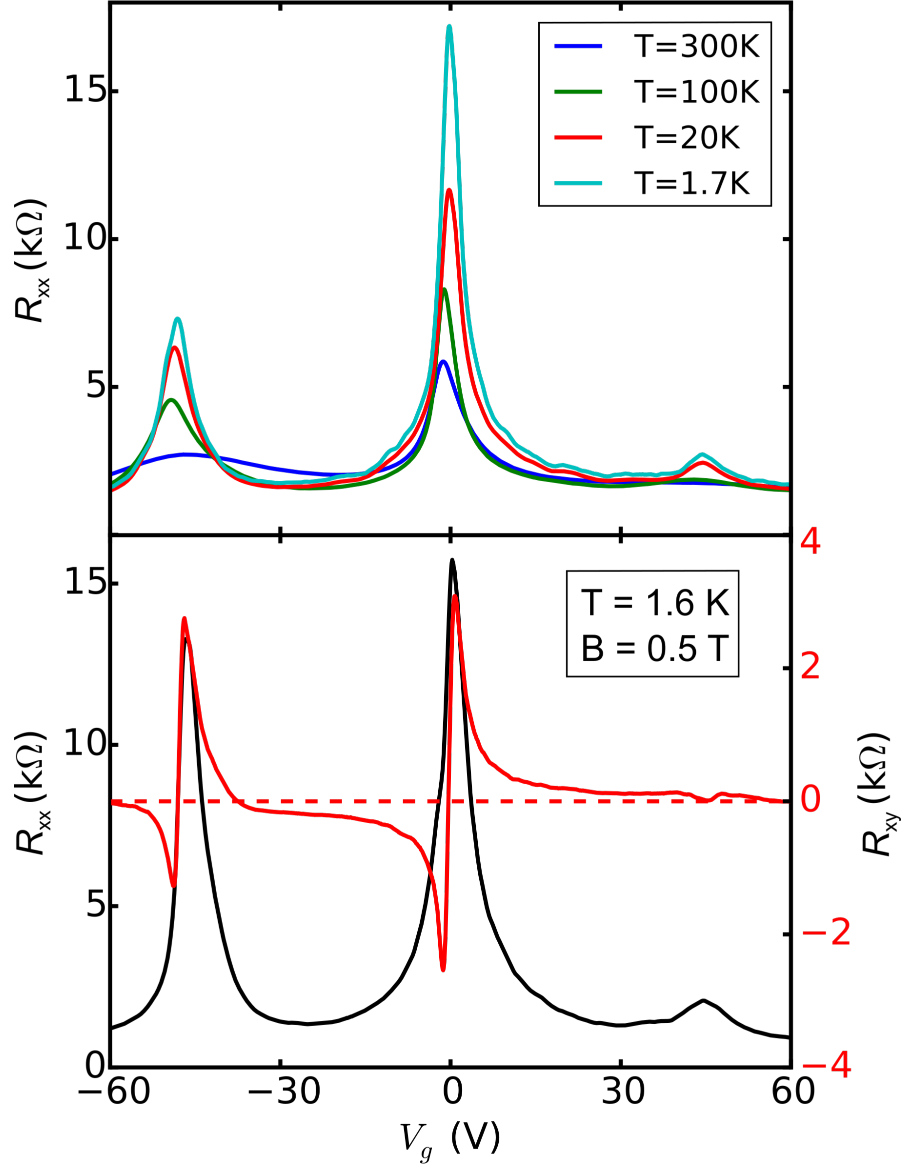

Figure 2.2: Transport signature of moiré minibands. Top: Temperature dependence of longitudinal resistance R_{xx} versus gate Voltage V_g. There are three resistance peaks observed including one at charge neutrality point (mDP) and two at symmetric electron and hole doping levels, which arise from sDP generated by minband. Bottom: R_{xx} (left axis) and Hall resistance R_{xy} versus V_g at $B = 0.5$T and $T = 1.6$K. The Hall resistance shows sign changes at mDP as well as sDP, indicating electron- and hole-like states near the moiré minibands.

In order to observe the miniband effects in a transport measurement, graphene has to be doped so that the Fermi level reaches the sBZ edge

$$E = \hbar v_F b/2, \tag{2.2}$$

where $b = 4\pi/\sqrt{3}\lambda$ is the sBZ reciprocal lattice constant. This translates to a carrier density of $n_s = 4\pi/3\lambda^2$. The gate voltage needed for typical 300nm SiO_2 gating with a capacitance per unit area $C_g \approx 11.5\text{nF/cm}^2$ to reach n_s for a perfect aligned graphene/hBN superlattice is ~30V. Because of the sharp dependence of wavelength on rotation angle, the gate voltage required to reach n_s quickly increases to ~60V for $\theta = 1°$ and ~147V for $\theta = 2°$. In an experiment, this restricts the rotation angle to be $\sim 1°$. For such practical reasons, only ~3% of randomly stacked graphene/hBN samples show transport signatures of minibands features.

While most of our graphene/hBN samples do not show any miniband features within the gate voltage range we can measure, our first sample that exhibited the unusual behavior was made serendipitously and the first dataset was taken in December 2012. Figure 2.2 plots the transport characteristics for an aligned sample. Figure 2.2a shows the longitudinal resistance (R_{xx}) vs. gate voltage (V_g) at four different temperatures. Clearly at $V_g \approx 0$V, a sharp resistance peak is observed corresponding to the main Dirac point (mDP) of graphene's electronic spectrum. Quite interestingly, there are two additional peaks in R_{xx} at symmetric electron and hole doping, these are features coming from the moiré minibands corresponding to the minima in the density of states. Figure 2.2b plots R_{xx} and Hall resistance (R_{xy}) versus V_g at T=1.6K and B=0.5T, in which R_{xy} changes sign at the mDP as well as the other two resistance peaks indicating new generation of Dirac points (sDP).

2.3 Hofstadter's Butterfly Spectrum in Graphene/hBN Superlattice

Electrons in a periodic lattice are described by Bloch bands/Bloch wavefunctions with a relevant length scale of the lattice constant a. On the other hand, when electrons are subject to a strong magnetic field, electronic spectrum are quantized to discrete energy levels called Landau Levels (LLs). The relevant length scale is magnetic length $l_B = \sqrt{\hbar/eB} \approx 25.7\text{nm}/\sqrt{B}$, where $\hbar$ is Plank's constant divided by 2π, e is electron charge and B is magnetic field in Tesla. When the relevant length scales a and l_B become commensurate, the interplay between the two length scales produces a complex energy spectrum known as Hofstadter's butterfly[50], theoretically predicted by Douglas Hofstadter back to 1976.

For a typical crystal, the lattice constant is on the order of ~1nm, the commensuration condition $a \sim l_B$ requires magnetic fields B ~1000T exceeding the limits of most research apparatus. Recent advancements in stacking graphene on high quality hBN crystals[41] makes the system an ideal candidate for studying this intriguing phenomenon-Hofstadter's butterfly owing to:

1. long superlattice wavelengths up to 14nm;
2. atomically smooth potential modulation as compare to periodic metal gates[51, 52];
3. high quality electronic performance (mobility reaches ~100,000cm^{-2}/V·s).

The Hofstadter's butterfly is essentially a fractal spectrum, in which the Bloch bands and LLs are split when the magnetic flux ϕ through a unit cell of the periodic

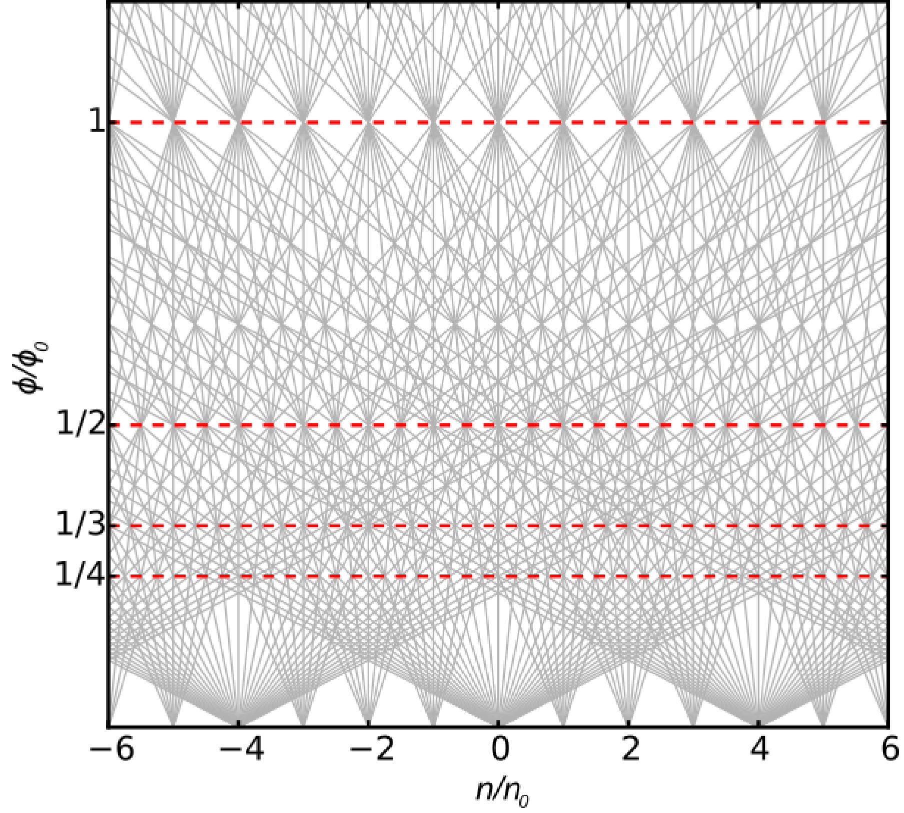

Figure 2.3: Diophantine diagram. Each grey line represents a pair of (t, s) values in the Diophantine equation. The red dashed lines correspond to $\phi/\phi_0 = 1$, $1/2$, $1/3$ and $1/4$, near where gapped trajectories with non-zero s had been previously reported.

lattice is a rational fraction of the flux quanta $\phi_0 = h/e$, i.e.:

$$\frac{\phi}{\phi_0} = \frac{p}{q}, \tag{2.3}$$

where p, q are co-prime integers. The splitting produces a self-replicating fractal spectrum, namely each Bloch band splits into q subbands or equivalently each LL splits into p subbands. Wannier[53, 54] further showed that energy gaps in the Hofstadter's spectrum in a density-field diagram can be described by the Diophantine relation

$$\frac{n}{n_0} = t\frac{\phi}{\phi_0} + s, \tag{2.4}$$

where n is charge density, n_0 is the density of one electron per unit cell and t,s are integers. Plotting the above equations with different t and s values produces a complex

diagram (Fig. 2.3). Noted that for $s = 0$ the Diophantine equation is reduced to $t = nh/eB$, t is exactly the filling factor ν in a Landau fan diagram. For non-zero s, gapped trajectories near $\phi/\phi_0 = p/q$ in the Diophantine equation had been previously reported in aligned graphene/hBN samples[6, 8, 55].

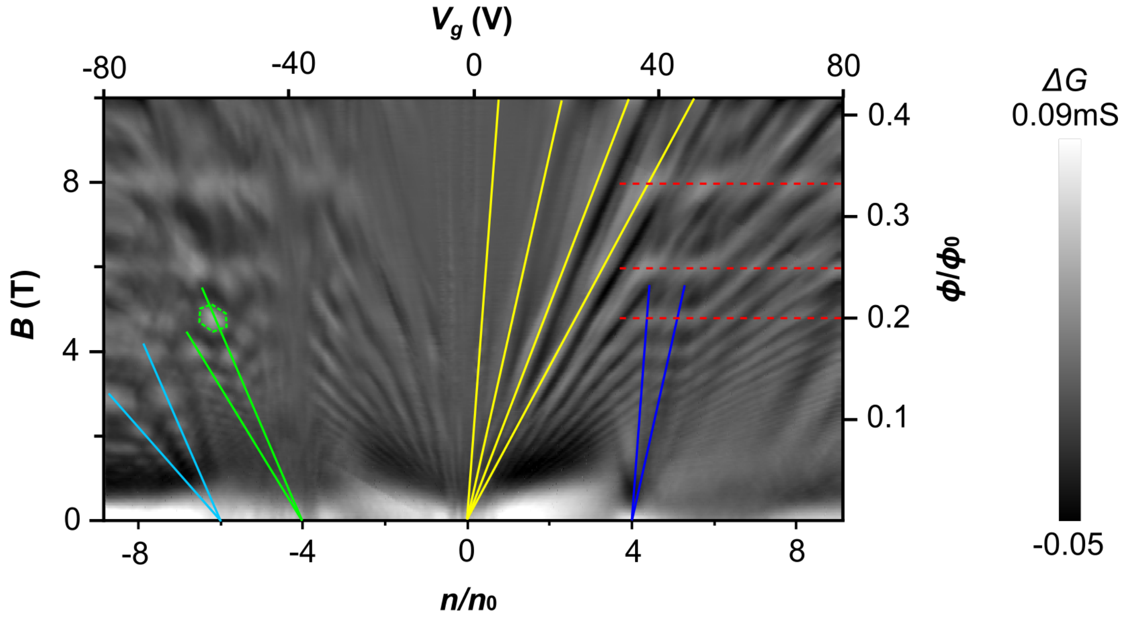

Figure 2.4: Conductance map in the density-field plane. Gray scale of background subtracted G (ΔG) vs. gate voltage (top axis)/normalized charge density (bottom axis) and B (left axis)/flux quanta per unit moiré superlattice unit cell (right axis). Yellow lines: Landau fan features originating from the mDP, $s = 0$. Blue lines: Landau fan features from the electron side sDP, relative $s = 0$. Green lines: Landau fan features originating from the hole side sDP, relative $s = 0$; green polygon: features created by the intersection of different s values. Cyan lines: Landau fan features originated from a relative $s = -2$ to with respect to hole side sDP. Red dashed lines: features parallel to the density axis at rational fractions of ϕ/ϕ_0.

For a graphene/hBN superlattice, electrons are subject to both the carbon lattice and the superlattice making the density-field behavior even more complex, a combination of the superlattice's Diophantine diagram and graphene's Landau fan diagram. Figure 2.4 plots the conductance (a smoothed background is subtracted to enhance visual contrast) of an aligned device in a two-terminal geometry. A rich and complex fan diagram is observed. The yellow lines correspond to the Landau fan features originating from the mDP. Blue and green lines follow the fan features from the sDP for electron and hole doping. These features are all coming from a relative $s = 0$ in the Diophantine relation. Interestingly, features originating from nonzero s are also visible, for example those along the cyan lines with a relative $s = -2$ from the hole side sDP. The intersection between features from different s values on the hole side produces a network of polygon features, one of which is outlined in the green dashed hexagon. Moreover, there are flat features parallel to the density axis along the red dashed lines at exactly rational fractions of ϕ/ϕ_0, which was reported previously[49].

The above features only highlight a few observations of the rich spectrum, while a better understanding of the physics of these features will require much more experimental and theoretical work. In chapter 4, we will present more data and analysis on this system.

Chapter 3

Sample Preparation and Device Fabrication

In this chapter, I will describe in detail some essential techniques for fabricating graphene devices, including:

1. Isolation and identification of graphene.
2. Transfer technique for stacking layered materials.
3. Fabrication of hBN supported or encapsulated graphene devices.

At the end of the chapter, I will discuss and compare the electronic quality of graphene devices on SiO_2 and hBN substrates as well as BN/G/BN encapsulated devices.

3.1 Sample Isolation and Identification

Graphene flakes are isolated from bulk material using the well known “Scotch tape method”, which was first introduced by Novoselov and Geim[1]. The technique is

also available for watch on Youtube: Graphene 101. In summary, the procedure can be divided into the following steps:

1. Substrate preparation.

    (a) Cut small SiO_2/Si chips (4 by 4 mm squares) from a large (5 inch) wafer.

    (b) Clean the silicon chips by sonicating in acetone for $\sim$ 20 minutes.

    (c) Rinse with IPA and blow dry them with N_2 gas.

2. Crystal cleavage.

    (a) Attach a piece of kish graphite or HOPG (Highly Ordered Pyrolytic Graphite) to a piece of Scotch tape.

    (b) Fold and unfold the tape around the edge of the graphite multiple times until the graphite is thin enough and distributed uniformly on the tape.

    (c) Put the tape with graphite on top of the clean silicon chip and gently press it to squeeze out air bubbles underneath the tape. Then, slowly pill the tape off the substrate. Some of the graphite flakes will be transferred to the substrate due to van der Waals interaction.

3. Flake identification.

    Search for thin graphene flakes under optical microscope. To optimize the speed and yield of finding graphene, a $\times 20$ objective is chosen. When a candidate flake is chosen, a larger objective can be used for better visualization. Figure 3.1 shows an example optical image of single and few layer graphene on 290nm SiO_2/Si substrate, where single, double and triple layers are labeled as 1L, 2L and 3L respectively.

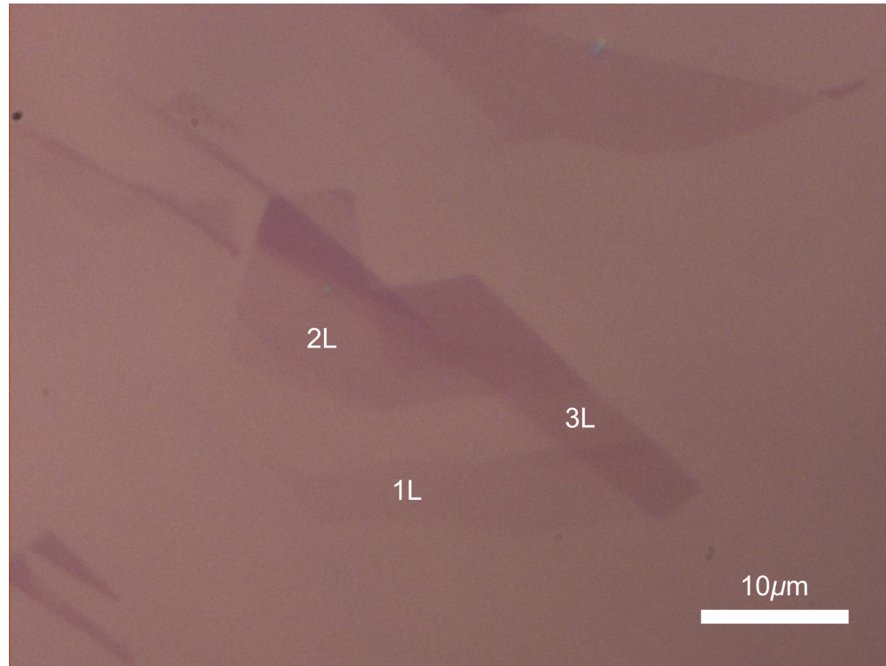

Figure 3.1: Optical image of single and few layer graphene on 290 nm SiO_2/Si substrate.

People might have created graphene long before 2004, but until then no one observed it with a typical optical microscope. It is really the simplicity of the tape folding method and optical visibility that have inspired the extensive research on graphene. One of the key steps of being able to see graphene optically is the right choice of substrate. P. Blake[30] numerically showed that the visual contrast of graphene on SiO_2/Si substrates depends both on the thickness of SiO_2 and wavelength of light, with optimal thickness of about 90nm and 290nm for green light.

Once the graphene is optically identified, we can then further characterize it and measure the number of layers using AFM (Atomic Force Microscopy). Figure 3.2 is an AFM image of the graphene shown in Fig. 3.1.

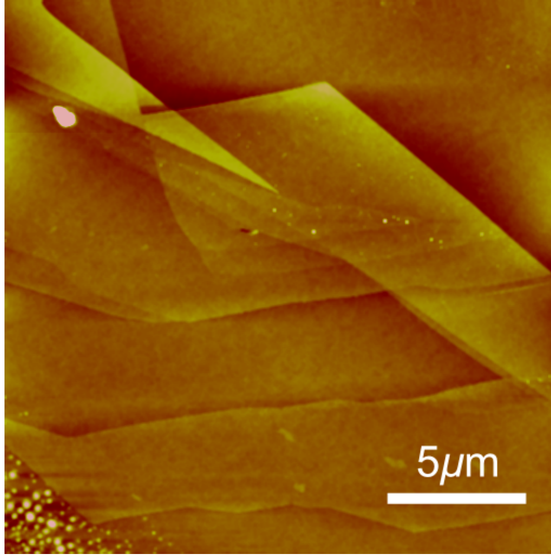

Figure 3.2: AFM image of single and few layer graphene on SiO_2/Si.

Another way of determining the number of graphene layers is via Raman spectroscopy[56], distinguished by the G and 2D peak strength and peak shapes. The quantum Hall effect[1, 10]can also be used to differentiate graphene layers resulting from the fact that different layers of graphene have different sequence of Hall plateau values. For example, single layer of graphene has Hall plateau sequence of $\pm(4n+2)e^2/h$ and bilayer graphene has plateau sequence of $\pm(4n+4)e^2/h$, where n is a non-negative integer. While the optical image is relatively faster and easy to use, the AFM, Raman spectroscopy and quantum Hall effect approaches are more accurate for determining the number of layers.

3.2 Mechanical Transfer of Graphene and Other Layered Materials

While exfoliating graphene on SiO_2/Si substrate is the most straightforward way to get started with, it is often desirable to have graphene on other substrates or on a

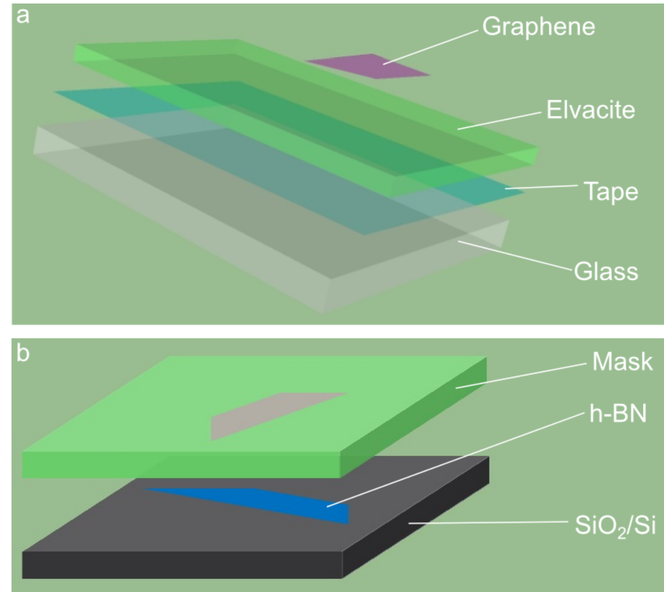

Figure 3.3: Illustration of the transfer method. (a) Schematic of the transfer mask. (b) Alignment of graphene with hBN.

particular location of a substrate. For instance, people have demonstrated that graphene supported by hBN exhibited mobility above 100,000 $cm^2/V{\cdot}s$[41] and micrometer scale ballistic transport at room temperature when graphene was encapsulated between two hBN layers[57]. However, direct exfoliation will not work in such scenarios because the size of hBN flake is typically smaller than 50μm. In this section, I will introduce a method that can position graphene onto any substrates with lateral accuracies down to about 5μm. Such a method can also be applied to transferring other layered materials such as MoS_2 and even carbon nanotubes.

3.2.1 Resist Assisted Transfer of Graphene

To transfer graphene onto hBN substrates, we use a technique similar to the one described by Zomer[58]. Figure 3.3 is an illustration of transferring graphene to hBN. The detailed procedures are summarized below:

1. Prepare transfer mask.
    (a) Attach a piece of transparent tape (Scotch 600K6) onto a glass slide with the adhesive side on the glass. Squeeze out any bubbles.
    (b) Spin coat 2 layers of Elvacite 2550 (dissolved in methyl isobutyl ketone, 8g/50ml) at speed of 4000rpm. No baking is needed in this step.
2. Exfoliate graphene and hBN.
    (a) Exfoliate graphene on the transfer mask. Identify a desired flake and cut the transfer mask to a 2 by 2mm square with the graphene in the center. Cutting the transfer mask into a small piece is essential to achieve accurate alignment.
    (b) Exfoliate hBN on to SiO_2/Si substrate using a similar method used for exfoliating graphene. Thermally anneal the sample in O_2 gas at 500°C for 2 hours to remove any tape residues. Identify a hBN that is uniform and clean for later use.
3. Align graphene with hBN and release it.
    (a) Mount the SiO_2/Si chip with hBN onto a micro-manipulator (cartridge heater installed) and facing downward.
    (b) Place the transfer mask with graphene on top of a inverted microscope (Zeiss Axiovert 200 MAT) and facing up.
    (c) Align the graphene and hBN by adjusting the micro-manipulator. Lower the hBN until it make good contact to graphene.
    (d) Heat the sample up to 60°C and wait for about 3 minutes.
    (e) Raise the micro-manipulator to release the Elvacite polymer onto the SiO_2/Si substrate due to a stronger adhesion than the transparent tape.

(f) To further assist graphene staying on hBN, bake the chip on hot plate at 150°C for 20 minutes.

4. Remove the resist and clean the sample.

   (a) Put the chip in Acetone on hot plate (60°C) for 10 minutes to remove Elvacite resist. Rinse with IPA and blow dry the sample.

   (b) To further remove any polymer residue, anneal the sample in O_2 at 300°C for 2 hours. This step also helps to reduce bubbles between graphene and hBN.

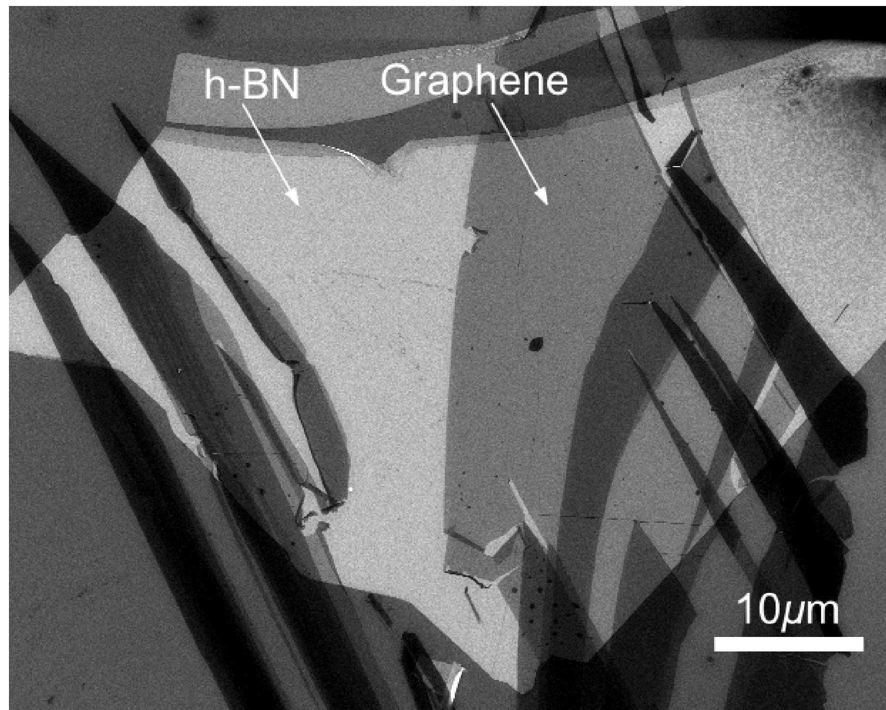

Figure 3.4: SEM image of a transferred graphene on hBN.

Figure 3.4 shows a SEM image of a transferred graphene on hBN. The brighter area is hBN, where graphene is usually darker with increasing layers.

3.2.2 Resist Free Transfer Technique

While resist assisted transfer provides a fast and high yield method to place graphene on alternative substrates, it usually leaves a layer of resist residue on it which is a source of contamination and potentially limits the quality of graphene devices. As a result, thermal annealing[41] or mechanical cleaning[59] after the device fabrication is required to remove resist residues. However, those procedures can potentially cause damage to the devices. In our experience, annealing graphene/hBN devices at 300°C usually downgrades contact resistance to ∼100kΩ and sometimes the devices become insulating although other groups did not report such problems[41, 60, 61]. Nevertheless, even if no damage would be produced, it is hard to completely remove all the residues[62, 63]. As a result, it is desirable to have a transfer method such that graphene never contacts any resist. In 2013, Wang[64] pioneered a resist free transfer technique that utilized van der Waals forces between graphene and hBN to successively pick up additional layers and form sandwiched BN/G/BN structures. Transport measurements before and after thermal annealing indicated the device quality is the same and no cleaning procedure is necessary after fabrication. Furthermore, a low temperature mean free path of more than 15 μm was observed, possibly one of the best substrate supported graphene devices ever measured.

In Wang's work[64], they used a transfer mask that consists of a glass slide, a PDMS layer and a PPC (poly propylene carbonate) polymer layer. During the transfer, the mask was heated to ∼40°C for better adhesion. However, due to the low glass transition temperature of PPC (25 to 45 °C), it turns soft and can be easily broken during heating. In this section, I will describe a modified method combining the pick up technique[64] and the all-dry viscoelastic stamping technique[65, 66]. This method

is based on two facts:

1. When pulled off quickly from a substrate, layered materials (hBN, graphene) will stay on PDMS.

2. When pulled off slowly from a substrate, layered materials will be deposited onto the substrate.

Our transfer mask is simplified to a PDMS layer on top of a glass slide. To make the BN/G/BN sandwiched structure, we perform the following steps:

1. Mechanically exfoliate hBN to the transfer mask.

2. Select a uniform and clean hBN layer and aligned to the target graphene prepared on SiO_2/Si. Then, heat the sample to ~ 50°C and quickly pull off the mask from substrate to pick up the graphene.

3. Align the BN/G stack to another hBN layer sitting on SiO_2/Si and slowly pill off the transfer mask, leaving the BN/G/BN sandwich on the target substrate.

Our modified method involves no resist polymer at all which greatly reduces the process time of spin coating and resist cleaning. Furthermore, the transfer mask can be recycled multiple times. Figure 3.5 shows the optical image of an example BN/G/BN structures.

In summary, we have demonstrated two transfer methods, including resist (Elvacite) assisted transfer and resist free transfer. In practical experiments, one can choose accordingly which method to apply depending on their needs. When yield is more important, the resist assisted technique can produce samples faster. If device quality is the concern, one might want to try resist free transfer. One other method that involves

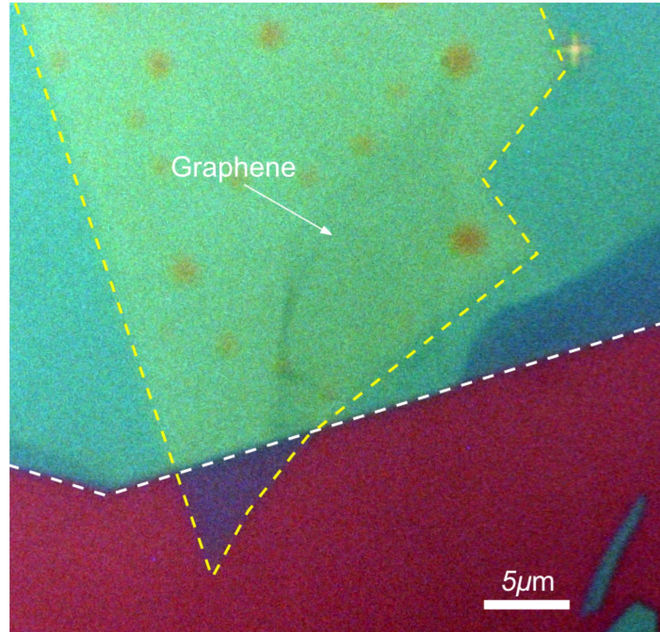

Figure 3.5: Optical image of a BN/G/BN sandwich structure. The shadow area in the center of the image is single layer graphene. The cyan color is hBN where the yellow and white dashed lines outline the bottom and top hBN layer respectively. The BN/G/BN structure lie on top of SiO_2/Si in red.

a wet process (wet etching of substrate) is widely used to transfer CVD (chemical vapor deposition) grown graphene to arbitrary substrates[67–69]. This method is also useful when pre-processing is needed, for example to transfer a complete device[70].

3.3 Fabrication Graphene Field Effect Transistors

In this section, we will first describe some of the essential techniques to fabricate high quality substrate supported graphene field effect transistors (FETs). Then, an innovative method of contacting graphene covered by hBN via an one dimensional carbon chain is introduced.

3.3.1 Fabrication of Graphene/hBN FETs

To fabricate graphene/hBN field effect transistors, we utilize standard electron beam lithography (EBL) and oxygen plasma etching[1] to define the device shape and electrodes. Then, electron beam evaporation and lift-off processes are used to metalize the device. The detailed recipe and procedure are listed below and the flow chart can be found in Fig. 3.6.

1. Etch graphene into Hall bar shape.

   (a) Spin coat the sample with a layer of PMMA (Microchem 950 A4) at a rate of 4000rpm for 40 seconds and bake it at 180° for 10 minutes.

   (b) Design etching pattern to open windows where graphene needs to be etched away. Expose the PMMA resist using EBL (LEO SUPRA 55 Scanning Electron Microscope) at a dose of $\sim 300\mu C/cm^2$. Develop in methyl isobutyl ketone/isopropyl alcohol (MIBK/IPA, 1:3) for 65 seconds and rinsing in IPA for 30 seconds.

   (c) Etch graphene in O_2 plasma with ICP (inductively coupled plasma) . Etching parameters (forward/ICP power, flow rate, time) are (30/300watts, 50sccm, 3 seconds). For few layer graphene (<4 layers), etching should only take less than 3 seconds.

   (d) Remove the PMMA resist in PG remover at 80°C for 2 hours and anneal the sample in furnace at 300°C for 2 hours. We found that these cleaning steps are crucial for achieving best contact resistance with graphene.

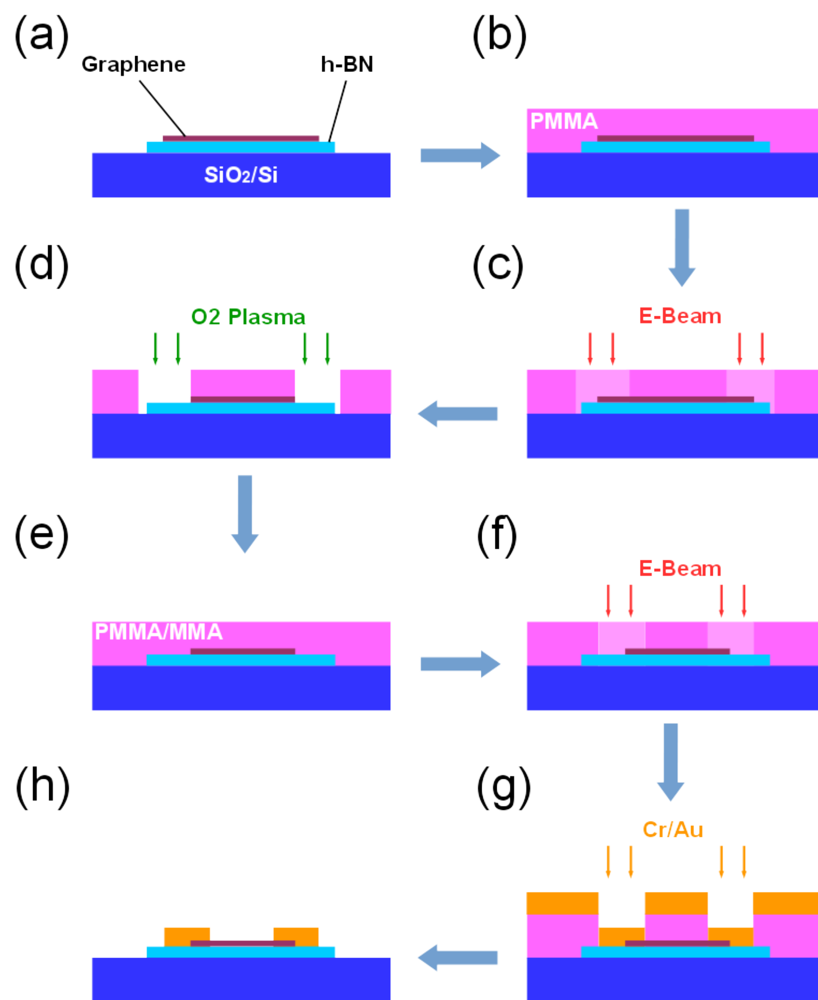

Figure 3.6: Flow chart of the fabrication procedure. (a) G/hBN sample on SiO_2/Si substrate. (b) Spin coat PMMA. (c) EBL to open window for etching. (d) O_2 plasma etching in ICP. (e) Spin coat PMMA (top)/MMA (bottom). (f) EBL to define electrodes. (g) Deposit Cr/Au metals. (h) Schematic of a complete G/hBN device.

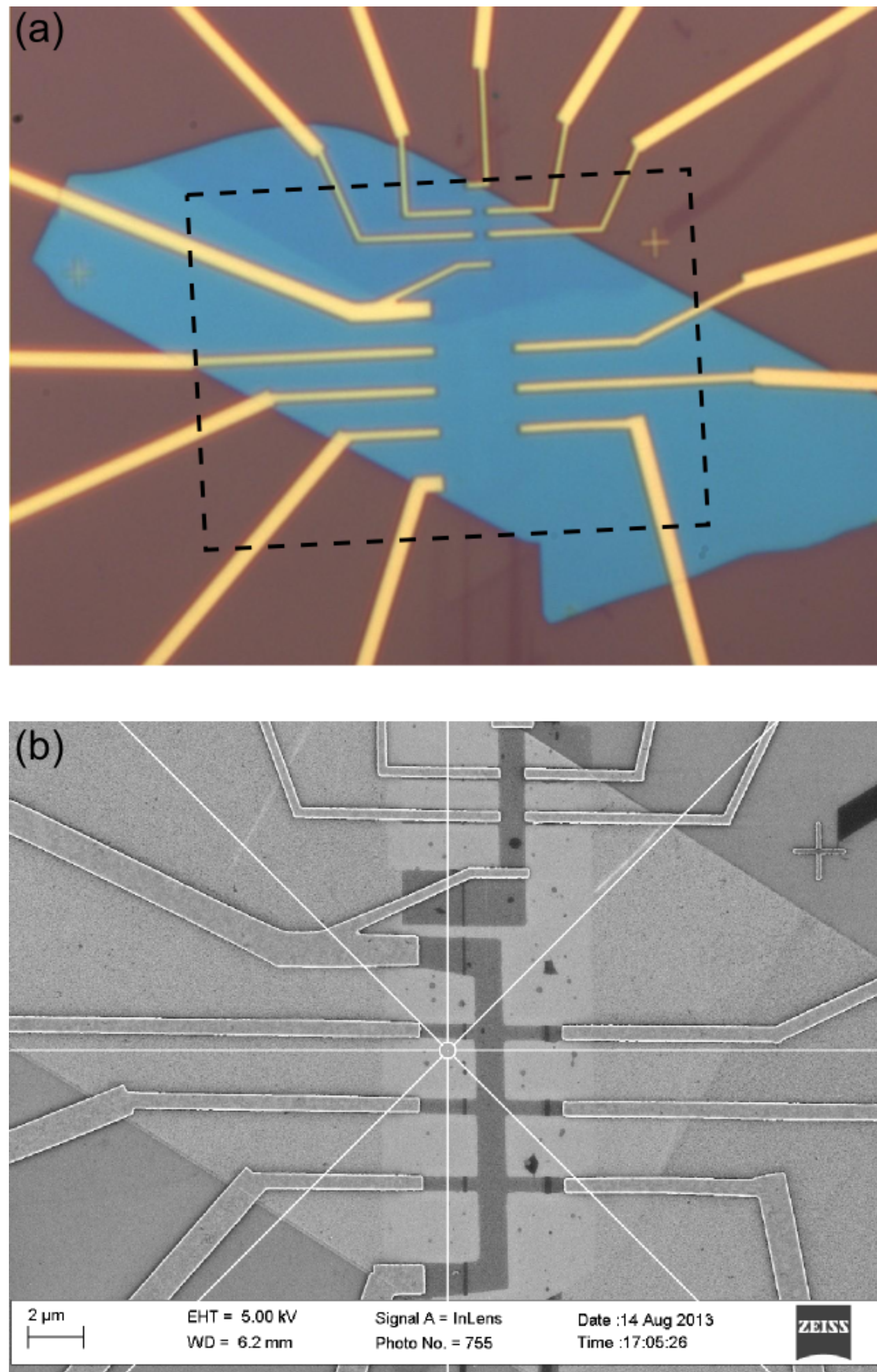

Figure 3.7: (a) Optical image of a complete G/hBN device. (b) SEM image of the same device corresponding to the dashed area in (a).

2. Define electrodes.

    (a) Spin coat the sample with bilayer resist PMMA (top)/MMA (bottom) at a rate of 4000rpm for 40 seconds. Bake the MMA layer at 150°C for 2 minutes and the PMMA layer at 180°for 10 minutes.

    (b) Expose the electrodes pattern using EBL at a dose of ~400 µC/cm^2. Develop in MIBK/IPA (1:3) for 65 seconds and rinsing in IPA for 30 seconds.

3. Metal deposition. Metals are deposited using electron beam evaporation (Temescal BJD 1800 system). We first deposit 1 nm of Cr as an adhesion layer following 80 nm of Au. The thickness of Au should be at least 20 nm thicker than the depth of the hBN layer. Finally, we place samples in Acetone on hot plate (65°C) for several hours to lift-off any unexposed PMMA/MMA resist and rinse with IPA/blow dry with N_2. Figure 3.7a and b show a optical image and SEM image of a complete G/hBN device.

3.3.2 Fabrication of Edge Contacts to Encapsulated Graphene

In the previous section, we have discussed a innovative technique that utilized van der Waals forces layered compounds to successively pick up graphene and hBN layers, resulting in a sandwiched BN/G/BN structures. However, it is challenging to electrically contact the graphene layer since it is fully covered by an insulating hBN layer. Wang demonstrated in their paper[64] that such contacts are feasible and the contact resistance can be as low as $\sim 100\Omega$. The most critical step to achieve good contacts is to etch through the BN/G/BN stack and expose a one dimensional chain of carbon atoms. The tools and procedure used are essentially the same as fabricating G/hBN devices except a few steps need to be taken care of. These points are summarized as follows:

1. After the etching windows being opened, etch the sample in SF_6 plasma in ICP (30/300 watts, 50sccm, 10 seconds).

2. Before depositing metal, functionalize the graphene edge with O_2 plasma in ICP (30/0 watts, 50sccm, 10 seconds).

3. The contact metals are made of Cr/Pd/Au with thickness of 1/3/100 nm respectively. The total metal thickness should be larger than that of the bottom hBN layer.

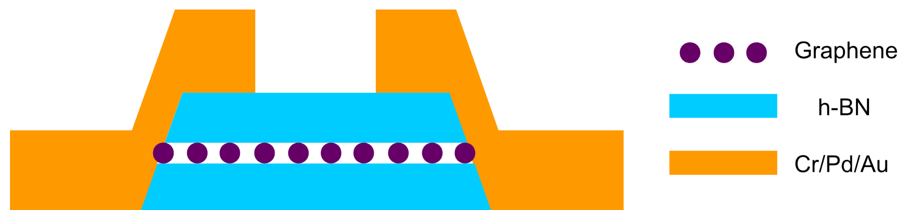

Figure 3.8: Schematic of metal contacts to graphene

The carbon atoms are exposed on the edge due to the sloped profile from ICP etching. A schematic of the cross section between BN/G/BN and metal contacts is show in Fig. 3.8.

3.4 Comparison of Electronic Qualities of Graphene Devices

In this section, we will compare the electronic qualities of our G/SiO_2, G/hBN and BN/G/BN devices in terms of carrier mobilities (μ).

For non-encapsulated graphene, we usually anneal our samples in flowing H_2/Ar (0.2slm/0.4slm) gas for ~2-4 hours to remove resist residues. For BN/G/BN samples, such cleaning process is unnecessary as the transport quality does not change much before and after annealing[64]. In order to compare the qualities of the devices, we calculate μ using two methods. The field effect mobility μ_{FE} is calculate from the slope of σ vs. n:

$$\mu_{FE} = \frac{1}{e}\frac{d\sigma}{dn}\,, \tag{3.1}$$

where e=1.6×10^{-19} C is the electron charge, σ and n are graphene sheet conductivity and carrier density. We also fit our data to a self-consistent Boltzmann equation which includes both long and short range scattering terms[34, 35, 41]:

$$\sigma = ((|n|e\mu_C + \sigma_0)^{-1} + \rho_S)^{-1}, \tag{3.2}$$

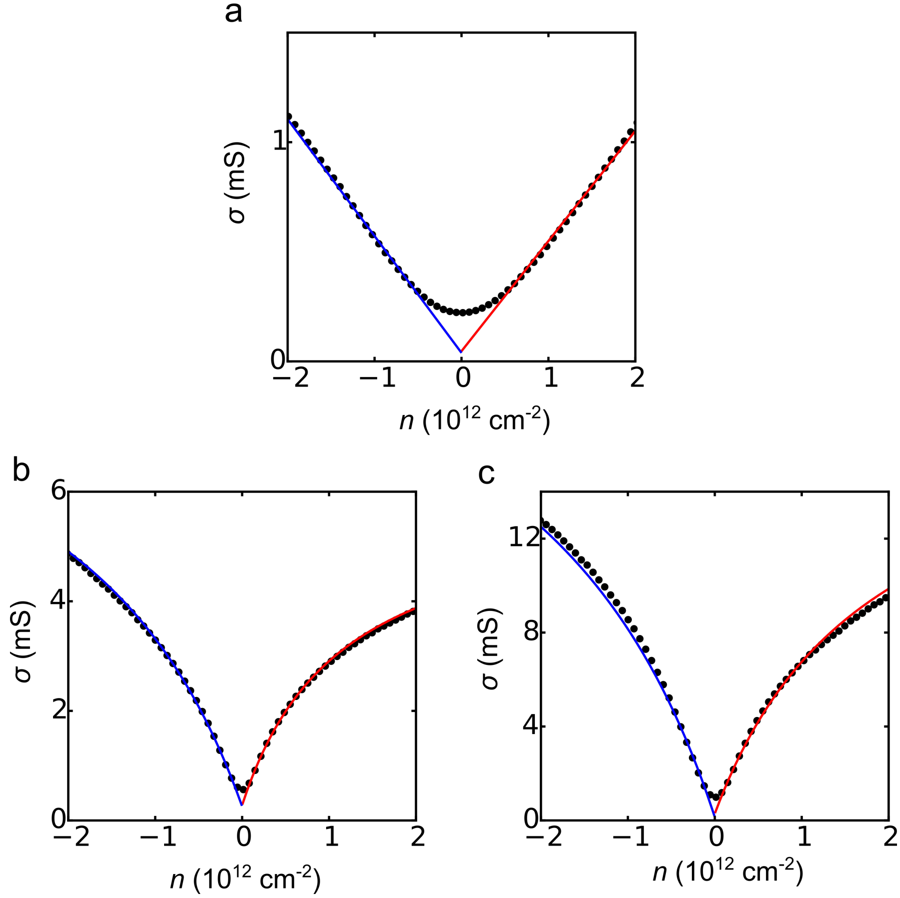

Figure 3.9: Transport characteristics for graphene devices at room temperature (300K). (a) σ vs. n for G/SiO_2 device. Black circles are experimental data and red/blue lines fitted curves to Equation 3.2 for hole/electron doping. (b) Same as (a) for a G/hBN device. (c) Same as (a) for a BN/G/BN device.

where μ_C corresponds to density-independent charged impurity scattering, ρ_S is short range scattering contribution, and σ_0 is residual conductivity at charge neutrality point (CNP). Fitting is carried out separately for electron and hole doping in observation of electron/hole asymmetry. Figure 3.9a, b and c plot σ vs. n for representative G/SiO_2, G/hBN, BN/G/BN devices with experimental data in black circles and fitted curves in colored lines. These data are all taken at room temperature (300K) in vacuum, low temperature data follow a similar trend. From the conductivity curves, we immediately

observe an increasing in transport quality from G/SiO_2, G/hBN to BN/G/BN devices. The μ_{FE} is calculated for low density and high density region. The μ_C is calculated separately for electron and hole doping. The quantitative results are summarized in Table 3.1.

device	μ_{FE} (cm^2/V·s)		μ_C (cm^2/V·s)	
	low n	high n	e	h
G/SiO_2	3500	3300	3100	3300
G/hBN	35000	10000	34000	29000
BN/G/BN	80000	18000	64000	72000

Table 3.1: Mobility values corresponding to Fig. 3.9.

Chapter 4

Topological Winding Number Change and Broken Inversion Symmetry in a Hofstadter's Butterfly

Abstract

Graphene's quantum Hall features are associated with a π Berry's phase due to its odd topological pseudospin winding number [9, 10]. In nearly aligned graphene-hexagonal BN heterostructures, the lattice and orientation mismatch produce a superlattice potential, yielding secondary Dirac points in graphene's electronic spectrum [6, 8, 44, 49], and under a magnetic field, a Hofstadter butterfly-like energy spectrum [6, 8, 49]. Here we report an additional π Berry's phase shift when tuning the Fermi level past the secondary Dirac points, originating from a change in topological winding number from odd to even when the Fermi-surface electron orbit begins to enclose the secondary Dirac

points. At large hole doping inversion symmetry breaking generates a distinct hexagonal pattern in the longitudinal resistivity versus magnetic field and charge density. Major Hofstadter butterfly features persist up to ∼100 K, demonstrating the robustness of the fractal energy spectrum in these systems.

Hexagonal boron nitride-graphene (hBN/G) heterostructures [41] have recently emerged as model systems for experimentally investigating the properties of electrons in a combined periodic potential and magnetic field [6, 8, 49]. Like graphene, the hBN atoms are arranged in a honeycomb lattice, but with a $\sim 1.8\%$ lattice constant mismatch. Graphene's band structure consists of two inequivalent gapless Dirac points in the Brillouin zone at which the valence and conduction band touch, with a pseudospin degree of freedom originating from the two atoms per unit cell. When placed on hBN, the lattice and orientation mismatch creates a periodic moiré pattern [6, 8, 44, 49], with a lattice-commensurate phase with periodic domains reported to form at small mismatch angles when the moiré period is $>\sim$ 10nm [71]. At special points at the edges of the superlattice Brillouin (sBZ) zone, the superlattice potential induces secondary Dirac points [6, 8, 44, 46, 47, 49, 71–75] and is predicted to open small gaps for both electron and hole states if inversion symmetry is broken [44, 46, 47, 72, 73, 75]. Under a magnetic field B, commensuration effects between the lattice period and the magnetic length lead to predictions of a fractal energy spectrum known as a Hofstadter's butterfly [50]. Recently such a spectrum appropriate for graphene's Dirac band structure [49] has been observed, as well as in bilayer graphene [6], and accompanied by the opening of a gap at the charge neutrality point [8, 71], opening the door to the exploration of this system. Compared to previous efforts on semiconductor heterojunction based two-dimensional electron gasses [51, 76–80], the graphene-hBN system is readily tunable, enabling the quantum Hall effect to be explored more fully [6, 8, 49].

Previously, magneto-transport [6, 8, 49] and capacitance [55] data were reported for densities where the Fermi level E_F was tuned beyond the secondary Dirac points, with two-terminal conductance data presented over an especially wide range in ref. [8]. However relatively little discussion or analysis was presented for this regime, especially at lower magnetic fields $<\sim 10$ T. Here, we focus on four-terminal measurements at large charge densities at such magnetic fields, enabling new phenomena to be identified. In the Hofstadter butterfly spectrum [53, 81–83], spectral gaps and minima in the longitudinal resistivity R_{xx} occur along lines in the density and magnetic field plane according to the Diophantine equation $(n/n_0) = t(\phi/\phi_0) + s$ with integer t and s. Here n is the carrier density, n_0 corresponds to one electron per superlattice unit cell, ϕ is the magnetic flux threading a superlattice unit cell, and $\phi_0 = 2\pi\hbar/e$ is the flux quantum with $\hbar$ Plank's constant, and e the electric charge. When $s = 0$, the integer t corresponds to filling factor $\nu = 2\pi n\hbar/eB$, and determines the slope of the gap features in the $n/n_0 - \phi/\phi_0$ plane for general s. The integer s determines the miniband from which the spectral gaps originate at $B = 0$. This behavior has recently been observed experimentally [6, 8, 49].

Here, we report that surprisingly, once the electron density is tuned past the secondary resistance maximum, the integers t corresponding to the R_{xx} minima for $s = 0$ become those of R_{xx} maxima and vice-versa. This can be understood as arising from an additional phase originating from graphene's Dirac particle spectrum in which the Dirac pseudospin winding number w, which counts the number of times the pseudospin rotates under a closed orbit [9, 10, 72, 84], changes from odd to even. The winding number is topological and reflects the total number of Dirac points enclosed by the orbit, each of which contributes ± 1 to the total w [72, 84]. The transition occurs when E_F is such that the semiclassical electron orbits enclose the additional odd number of the Dirac

points forming at the edge of the mini-Brillouin zone [46, 47, 72–74, 84], adding an additional relative phase of π accumulated in a single orbit, consistent with theory [72, 84]. This changes the observed filling factors where gaps occur to $t = 4m$ with $s = 0$, for integer $m > 0$, interchanging the R_{xx} maxima and minima at constant t, as observed. This demonstrates that such orbits, which require magnetic breakthrough of the Bragg scattering condition at the sBZ boundaries [85], are relevant to the observed behavior on the electron side.

In previous work on graphene bilayers changes in orbit topology and a Lifshitz transition at energy $E^* \sim 6$ meV were reported arising from pairs of degenerate Dirac points near the K and K' points, produced by an interaction-driven spectrum reconstruction [86]. In this work [86], however, no changes in the filling factors corresponding to spectral gaps were observed. In contrast, here the number of Dirac points enclosed by the Fermi surface orbit changes with Fermi level, enabling topological winding number changes to be observed.

For hole doping, where the lattice perturbs the charge carrier motion more strongly [47, 73, 75], the mixing between features originating from the different Bloch bands is stronger. Inversion symmetry breaking [71, 73] generates a distinct hexagonal pattern in R_{xx} vs. B and gate voltage V_g. Gaps at the hexagon centers occur at $t = 4m$, with $s = -4$, for integer $m < 0$, in accordance with theory [73]. New generations of Dirac particles are clearly observed, where peaks in R_{xx} are associated with sign changes in the Hall resistivity R_{xy} from positive to negative, consistent with previous studies [6, 49]. The honeycomb pattern shows that the Dirac points alternate with gaps in a systematic manner as the density and field are varied, demonstrating a regularity to the fractal spectrum in hBN-graphene similar to that proposed by Hofstadter [50].

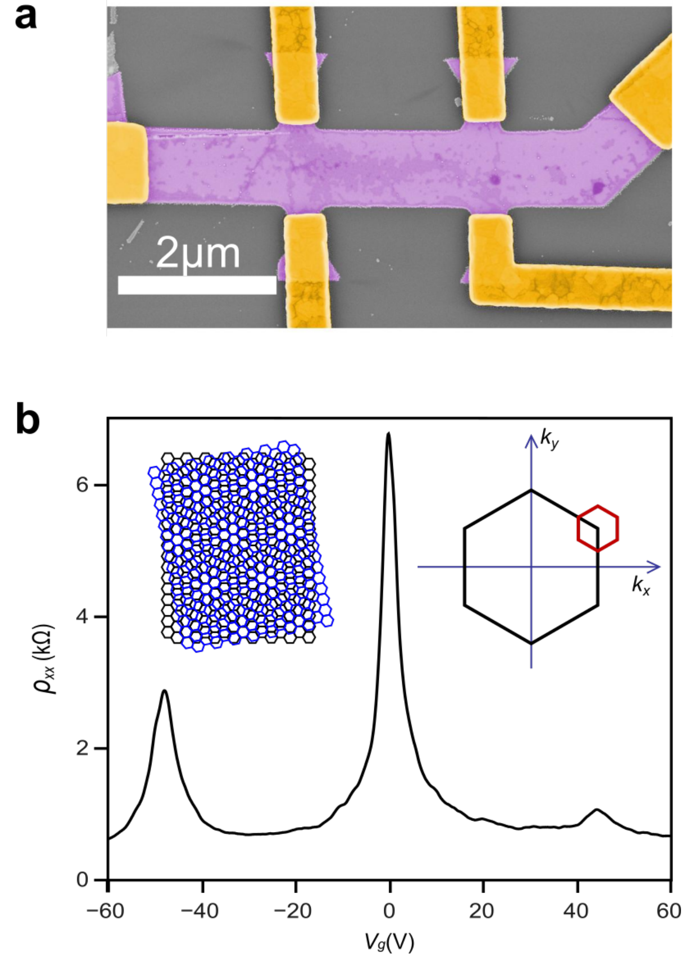

Figure 4.1: **hBN/G heterostructure device geometry and transport properties.** (**a**) Hall bar device. Graphene is crystallographically aligned and placed on a hBN substrate. The resulting structure is etched into a Hall bar geometry and leads are attached. (**b**) Longitudinal resistivity measured vs. gate voltage. Analysis yields a four-terminal electron mobility $\sim 9,000$ cm^2/V·s. Left inset, schematic of moiré pattern from stacked hBN and graphene layers. Right inset: schematic diagram of superlattice Brillouin zone (red hexagon) and its relation to the Brillouin zone of graphene (black hexagon).

Figure 4.1a shows a scanning electron microscope image of a completed device(G1), fabricated as described in the Supplementary Discussion. The four-terminal resistance vs. gate voltage V_g is shown at temperature $T = 1.5$ K in Fig 4.1b. The primary resistance peak near $V_g = 0$ when the device Fermi level is tuned through the charge neutrality point surrounded by two additional peaks. These peaks correspond to minima in density of states induced by the periodic potential from the moiré superlattice [6, 8, 44, 46, 47, 49, 73, 74], shown schematically in the Fig. 4.1b left inset, with the graphene lattice represented in black and hBN lattice in blue. The right inset of Fig. 4.1b shows the Brillouin zone of graphene in black, and the sBZ of the moiré superlattice in red around one of the corner points.

The evolution of the features in the main panel of Fig. 4.1b with magnetic field is shown in Fig. 4.2. Figure 4.2a shows R_{xx} vs. B and V_g, while Fig. 4.2b shows R_{xy}. Data is also plotted with respect to normalized density n/n_0 and ϕ/ϕ_0 (determined as described in Supplementary Discussion). A number of features are apparent. Minima in R_{xx} and plateaus in R_{xy} extend from the charge neutrality point. Similar features are also apparent extending from the secondary Dirac points on the electron and hole sides. The minima in R_{xx} originating from the primary Dirac point can be followed as they cross the Landau level like features from the secondary Dirac point on the electron side. Interestingly, for large filling factor ν, which corresponds to the integer t for $s = 0$, once the visible features extrapolating to the secondary Dirac point are crossed , the minima become maxima and vice-versa, for example as shown by the dotted line in Fig. 4.2a.

Figure 4.3a shows this more clearly by comparing plots of R_{xx} vs. ν on the left hand side of the sDP to those on the right hand side. The black trace is taken from Fig. 4.2a along the black line while the red trace is taken along the red line. R_{xx}

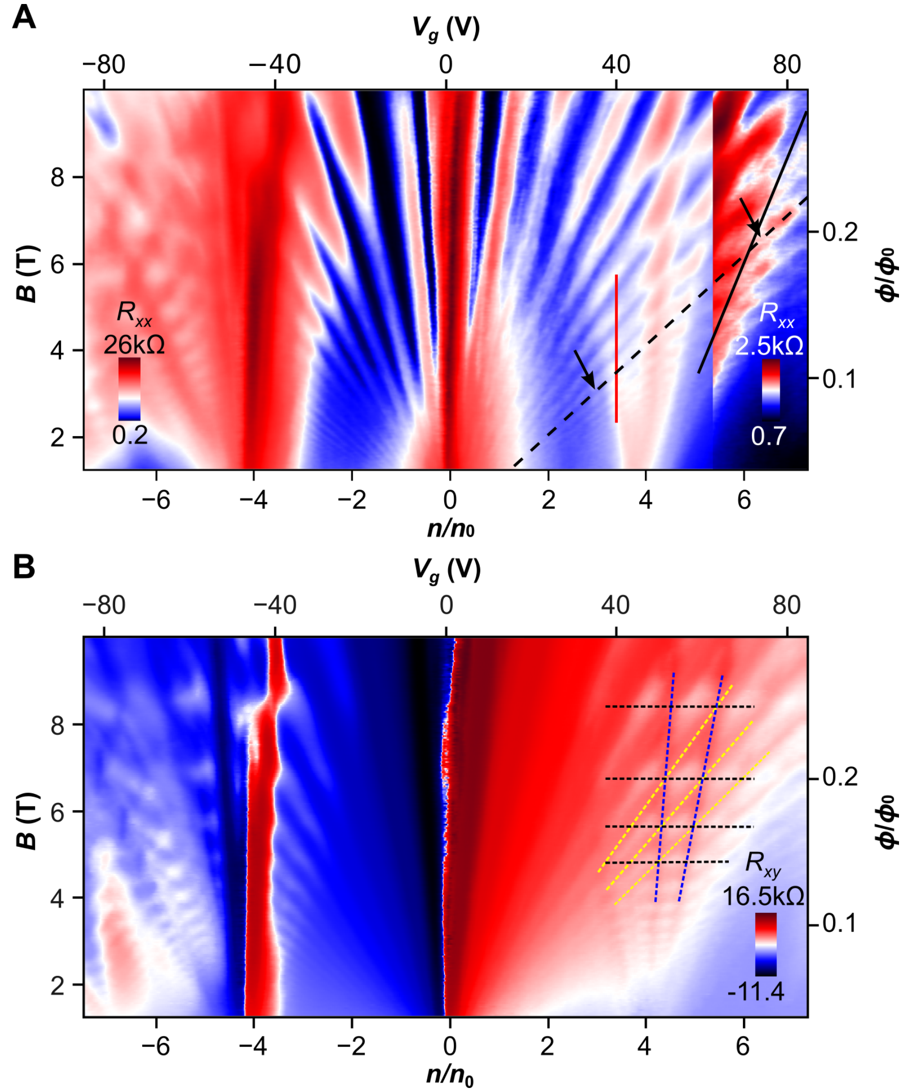

Figure 4.2: **Magnetotransport in a hBN/G heterostructure device.** (**a**) Color plot of R_{xx} vs. gate voltage (top axis)/normalized charge density (bottom axis) and B (left axis)/flux quanta per unit moiré superlattice unit cell (right axis). Data on right is plotted with enhanced contrast. Arrows correspond to regions where R_{xx} is at a minimum(lower left arrow) or a maximum (upper right arrow). (**b**) Color plot of R_{xy} vs. the same variables as in (**a**). Lines added on the electron side indicate Zak bands (black), and features corresponding to $s = 0$ (yellow) and $s = 4$ (purple) as a visual guide. Nonlinear color maps were used in (**a**) and (**b**) to enhance contrast.

oscillates with a period of 4 in both line traces but there is a π phase shift between them. Similar results were also found on a two-terminal aligned device G2 (Supplementary Information Fig. S4.1). The phase shift makes a transition at a given B over a range of V_g that increases with increasing B, as shown in Fig. S4.2, where an array of magneto-oscillation line traces at different V_g for G1 and G2 are shown versus ν. Figure S4.3 shows the oscillations and phase shift in V_g traces (plotted against ν) at an array of different B values, which shows that the phase shift is robust against uncertainties in the zero of charge. Here the phase shift occurs near a relative filling factor from the sDP of $\nu \approx 10$ for both samples. The transition region arises from the Zak minibands [49, 87]. that perturb the slope of the Landau fan features near $n/n_0 = 4$, especially in G2.

We can understand this by considering the motion of the electrons in an extended zone scheme of the sBZ. The quantum Hall states' filling factors at the R_{xx} minima can be determined semiclassically by the Bohr-Sommerfeld condition, from which it is found that the modulations in R_{xx} can be determined from the relation $\Delta R_{xx} = R(B,T)\cos[(2\pi(B_F/B + 1/2 + \beta)]$ [10, 28, 29], where B_F is the period of the oscillations in $1/B$, $R(B,T)$ is a pre-factor, and β is an additional topological phase accumulated over a single orbit, $\beta = w/2$. To compare to our data, we rewrite this in terms of ν, obtaining $\Delta R_{xx} = R(B,T)\cos[(2\pi(\nu/4 + 1/2 + \beta)]$, where the 1/4 factor multiplying ν stems from the spin and valley degeneracy in graphene. As was shown previously [9, 10], Dirac points in the spectrum have a topological number that determines the Landau level spectrum, which counts the number of times the pseudospin rotates under a complete orbit in reciprocal space [84]. Orbits that enclose a single Dirac point have a pseudospin winding number $w = \pm 1$ depending on whether they belong to the K

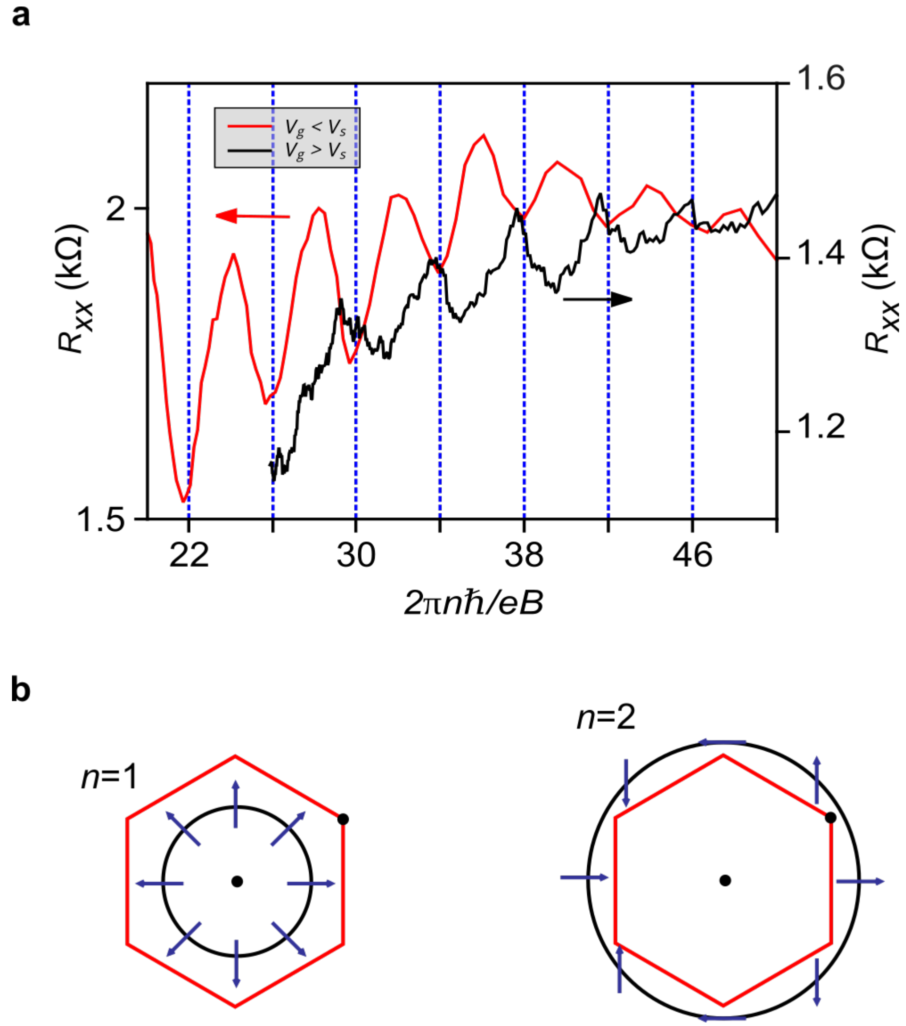

Figure 4.3: **Transition in Berry's phase and corresponding electron orbits.** (**a**) Plot of R_{xx} vs. filling factor $\nu = 2\pi n\hbar/eB$, for electron density below the sDP (red) and above (black), corresponding to the red and black lines in Fig. 4.2. (**b**) Semiclassical orbit (black) in reciprocal space shown in the sBZ (red). The pseudospin direction is shown by the blue arrow for the case of a winding number of 1 (top) and 2 (bottom).

or K' point or are in the valence or conduction band. Therefore, when the Fermi level is tuned below the secondary Dirac point encloses only the single primary Dirac point, resulting in a winding number of ± 1, β and an unconventional quantum Hall effect at filling factors ± 2, ± 6, ± 10 etc., corresponding to a Berry's phase of $\pm\pi$ as shown in Figure 4.3b top, consistent with previous studies [9, 10].

However, the situation differs when the Fermi level is tuned above the sDPs. Calculations indicate that the hBN induces either one or three Dirac points at the edges or corner of the sBZ depending on parameters, and has overshadowing bands [47], that may be viewed in a nearly free electron picture as the original Dirac spectrum folded into the sBZ. Electron orbits individually enclosing each of the secondary Dirac points could potentially occur via Bragg scattering at the sBZ boundary. However, interband tunneling via magnetic breakthrough to the overshadowing bands, expected to occur for relatively low fields $\phi/\phi_0 \sim 0.1$ [47], enables orbits that instead enclose the entire sBZ for sufficiently large doping, such as shown schematically in Fig. 4.3b bottom in an extended zone scheme. At the sBZ boundary, the theoretically expected number of Dirac points is odd; depending on substrate parameters there is one if it occurs at a corner of the sBZ, and three otherwise [47]. For the case of one Dirac point at the sBZ corner as shown in Fig. 4.3b, the winding number w changes to an even number, which yields $\beta = 0$ or ± 1, and an effective Berry's phase shift of 0 or $\pm 2\pi$, which is a relative phase shift of π compared to the low-doping regime. Three Dirac points at the sBZ edges would be expected to produce the same result. More detailed analysis [72] indicates that for an incommensurate lattice phase, an orbit enclosing the entire sBZ has $\beta = 0$, while the commensurate phase has $\beta = \pm 1$ with the bands becoming topological in nature, producing the same result. Thus, regardless of the substrate parameters, the R_{xx} minima and maxima vs. ν are exchanged, as observed.

Within the region defined by the most visible features of the sDP, the behavior is more complex. Horizontal feature alignments in R_{xy}, plotted in Fig. 4.2b, result from spectral gaps occurring at $\phi/\phi_0 = 1/q$, where q in an integer, arising from the Zak minibands [49, 87]. Additionally, R_{xy} oscillates as either a Zak band boundary (dashed black lines) or features corresponding to $s = 0$ (dashed yellow lines) or $s = 4$ (dashed purple lines) are crossed [6, 8, 49]. This can be interpreted as an interchange of electron and hole-like Landau level bands whenever a gap or Dirac point is crossed in the fractal spectrum, as expected from theory [47].

For large hole density a distinctive pattern of hexagonal ridges in R_{xx} emerges in the plot of R_{xx} vs. B and V_g. This is shown in Fig. 4.4a for a third sample G3 in which the hexagonal features were more clearly resolved. (An apparent charge inhomogeneity prevented an analysis of the phase shift on the electron side as was done for G1 and G2, as shown in Supplementary Information Fig. S4.4.) Measurement of R_{xy} shows a plateau at the minimum of the R_{xx} in the hexagon centers indicating the presence of a gap, as shown in Fig. 4.4b. At $B =\sim 5$ T, the field corresponding to the Zak band at $\phi/\phi_0 = 1/5$, a third generation Dirac point [6, 49] appears showing a peak in R_{xx} associated with a crossover from hole-like to electron-like behavior (Fig. 4.4c). We note that at other fields and gate voltages, the behavior in R_{xy} can be similar but offset from zero, consistent with previous work [6, 49]. The gaps at the hexagon centers occur along lines in the density-field plot that extrapolate to $n/n_0 = s = -8, -6$, and -4. The slopes of the lines are determined to follow $t = 4m$, where $m \neq 0$ is an integer with a sign determined by the extrapolation point. Calculations show that gaps occurring along lines with such slopes result from inversion symmetry breaking by the hBN layer [47]. Such inversion symmetry breaking may indicate the formation of a commensurate lattice phase [71]. The Dirac points occur along lines extrapolating to $n/n_0 = -4$ and -8 with

slopes $t = 4m + 2$, for integer m where the sign depends on s. No clear signature of magnetic breakthrough is observed, consistent with the calculated spectrum that shows larger gaps at the sBZ boundaries without overshadowing bands [47].

Finally, R_{xx} in the large hole doping regime vs. V_g and B is plotted at two additional temperatures in Fig. 4.4d. The Zak miniband structure persists up to at least 100K indicating an energy scale at least $E_Z \sim$10-30 meV for these features. The temperature dependence data of R_{xx} within one of the hexagonal gap regions is plotted as an Arrhenius plot in Fig. 4.4e. Analysis of the linear region of the plot yields a gap $\sim$0.2 meV. This value is uncertain due to the relatively small range of data above the saturation region. Moreover, the small value may, for example, reflect transport mechanisms such as variable range hopping. More work is required to determine accurately the gaps in this region.

In sum, we have measured graphene samples with a moiré pattern potential from an underlying hBN substrate. For the electrons, we observe an additional π shift in phase in the magnetoresistance oscillations when tuning the Fermi level past the secondary Dirac points, indicating a change in topological winding number and electron orbits that enclose an even number of Dirac points. When the substrate interactions are stronger as on the hole side, a distinct hexagonal pattern emerges in R_{xx} vs. B and V_g which results from gaps that form due to inversion symmetry breaking, systematically paired with the formation of third generation Dirac points. Finally, in the semiclassical theory of electrons in periodic potentials and nonzero magnetic field, the electrons can tunnel between real-space cyclotron orbits, forming energy bands. This leads to new quasiparticles that follow "hyperorbits" [85, 88], acting as if they are in a reduced magnetic field. The ability to realize this situation may enable such theories to be tested, for example in magnetic focusing experiments [89, 90].

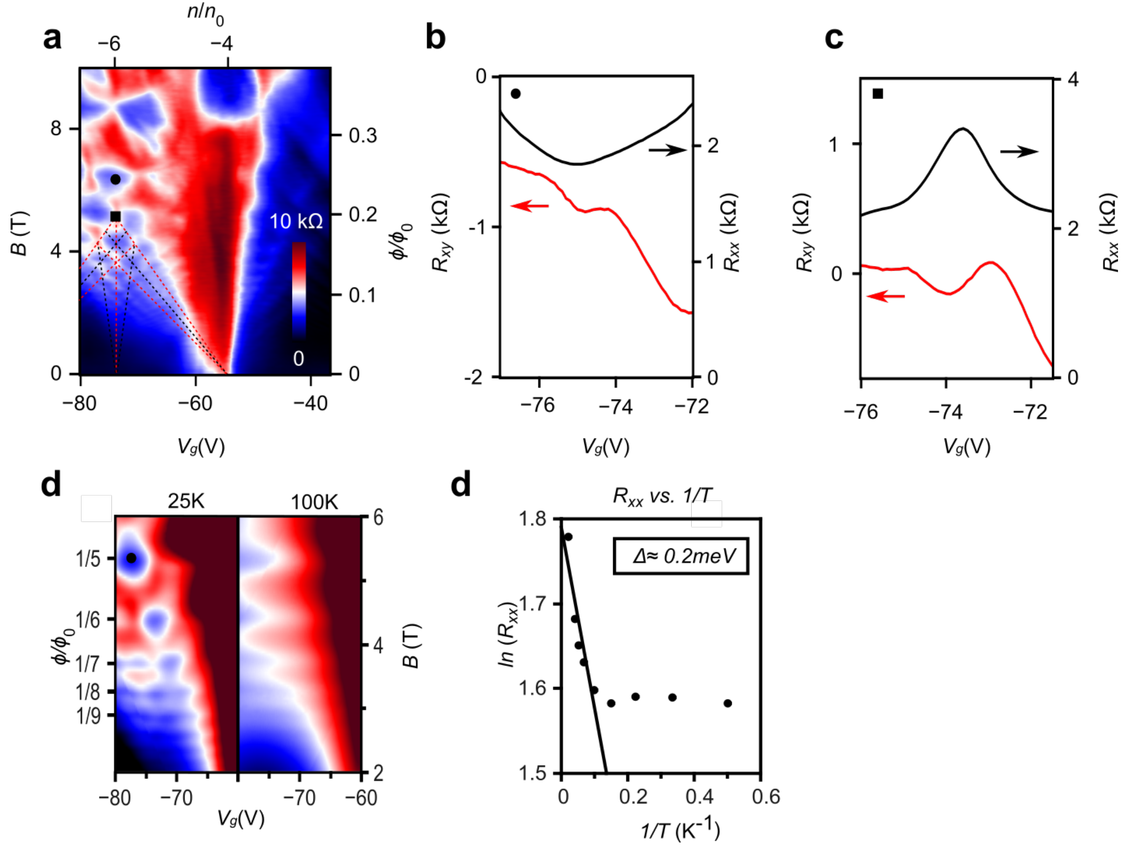

Figure 4.4: **Replica Dirac points and gaps in hole side.** (**a**) Color plot of R_{xx} vs. V_g (bottom)/normalized density (top) and B (left axis) flux quanta per unit moiré superlattice unit cell (right axis) near the sDP on the hole side showing hexagonal ridges for sample G3 with four-terminal mobility $\sim 20,000$ cm^2/V·s. A nonlinear color mapping was used to enhance contrast. (**b**) R_{xx} (black) and R_{xy} (red) vs. V_g taken near the point indicated by the solid circle in (**a**). (**c**) R_{xx} (black) and R_{xy} (red) vs. V_g taken near the point indicated by the solid square in (**a**). (**d**) region to the left of the sDP at $T = 25$K and $T = 100$K. Dark blue corresponds to 3 kΩ, and dark red to 9 kΩ. (**e**) Arrhenius plot of R_{xx} at the point indicated by the solid circle in (**d**).

S1. Sample Fabrication

Samples are fabricated by placing graphene on hBN using Elvacite 2550 layers [10], on top of an oxidized Si wafer with 300 nm oxide. The doped Si acts as a back gate. The edges' cleavage planes are oriented to within approximately $\sim 1°$under an optical microscope [8, 9, 44]. Raman measurements are used to verify the lattice alignment [6, 49], and electrodes are attached using electron-beam lithography.

S2. Parameter Normalization

To plot the data in terms of n/n_0, we determined n by measuring the Shubnikov-de Hass oscillations in R_{xx} at low B field using a range of densities near the secondary Dirac point. The density n_0, which corresponds to one electron per superlattice unit cell, was then extracted from the oscillations in R_{xy} that are independent of gate voltage near the secondary Dirac point called "Zak oscillations" [8]. Contours of these are shown by the black dashed lines in Fig. 4.2b of the main text. This enables the normalized density n/n_0 to be computed, which can be determined for the extrapolation point to $B = 0$ of the Landau fan features from the secondary Dirac Point (sDP). These occur at $n/n_0 = \pm 4$, consistent with previous studies [8, 9, 44]. From the normalized density, the area of the morié unit cell $1/n_0$ is used to determine the normalized magnetic field ϕ/ϕ_0, which is the number of flux quanta per superlattice unit cell.

S3. Two-terminal magnetotransport data for sample G2

We show in Fig. S4.1 magnetotransport data for a two-terminal aligned device G2 that exhibits secondary Dirac point features. The graphene/hBN alignment was confirmed by Raman spectroscopy [6, 49]. Figure S4.1a plots the two-terminal conductance versus B and V_g. Following the Landau fan features corresponding to a conductance minimum along constant filling factor ν (for example along the black dashed line) originating from the main Dirac Point (mDP), the conductance makes a transition to a maximum upon

crossing through the sDP at $n/n_0 = 4$ on the electron doped side, indicating a π shift in the magneto-oscillations vs. ν. Although only a single magnetic field direction was measured for this sample, symmetry in B is expected based on Onsager symmetry.

To improve the feature contrast, in Fig. S4.1b we plot the conductance with a smoothed background subtracted, labeled ΔG. At low densities the features are somewhat irregular, and curve towards the density axis at the lowest densities. This may be due to a combination of quantum interference phenomena [41] and insufficiently screened charge puddles [47, 71, 72]. However, above $n/n_0 \approx 2$, the Landau fan features are relatively regular and follow approximately straight lines. As in the previous plot, ΔG changes from a minimum to a maximum along lines of constant filling factor such as the back dashed line. To confirm that the background subtraction does not create any spurious or extra features in our data, we plotted line traces (along the red and black lines) from both the original data and background subtracted data versus filling factor in Fig. S4.1c and d. Both Figures show a similar transition of the magneto-oscillation phase as the minima from the left of the sDP (red line) align with the maxima from the right of sDP (black line).

For both devices G1 and G2, the onset of the region where the oscillation phase makes its transition occurs at $n/n_0 = 4$, where the miniband states are just filled, indicating that the observed behavior stems from the superlattice potential. Also, features from $n/n_0 > 4$ and those with similar slope from $n/n_0 < 4$ extrapolate back to the same point at $B = 0$, indicating that the shift in phase cannot be accounted for by a charge offset due to a charge inhomogeneity within the sample (see device G3 below).

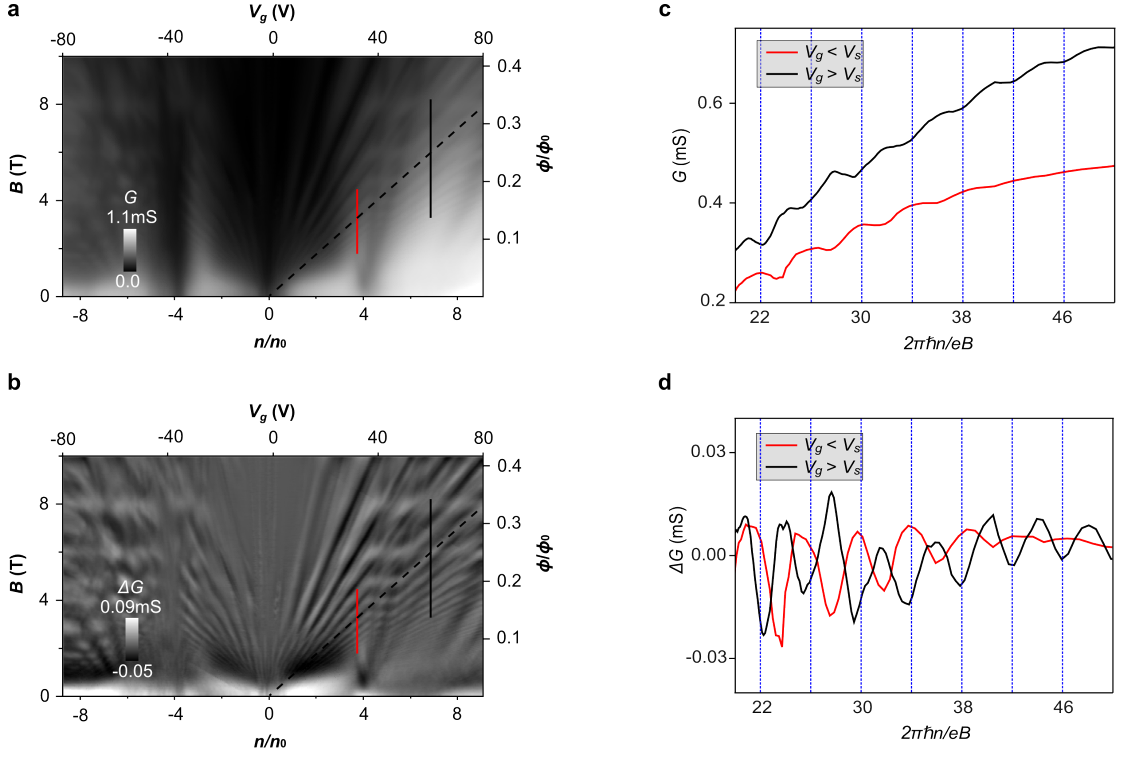

Figure S4.1: **Data for sample G2.** (**a**) Gray scale of G vs. gate voltage (top axis)/normalized charge density (bottom axis) and B (left axis)/flux quanta per unit moiré superlattice unit cell (right axis). (**b**) Gray scale of background subtracted G (ΔG) with the same axes as in **a**. (**c**) Plot of G vs. filling factor $\nu = 2\pi n\hbar/eB$, for electron density below the sDP (red) and above (black). (**d**) Plot the ΔG vs. ν for electron density below the sDP (red) and above (black).

S4. Additional vertical line traces showing the phase shift for sample G2 and G1

In order to better illustrate the π phase shift, we show here numerous line traces in a wide range of gate voltages covering the sDP for two devices G2 and G1.

In Fig. S4.2a, we plot ΔG vs. ν for device G2 with V_g ranging from 30V to 60V (1V increment) with the sDP feature around $V_g = V_{sDP} \sim 36$V. The traces are offset vertically for clarity. The minimum or maximum features stay at constant ν at low($V_g \ll V_{sDP}$) or high ($V_g \gg V_{sDP}$) gate voltages (blue and dashed lines) while shifting when $V_g \sim V_{sDP}$ (red dashed lines). Comparing the low to high gate voltage curves, the minima at low gate voltages align for the same ν with maxima at high gate voltages, demonstrating the π phase shift.

The transition region near $V_g \sim V_{sDP}$, becomes broader for lower ν, due to the Zak oscillations (horizontal bands in Fig. S4.1a) that perturb the slope of the features, which become wider in gate voltage at larger B. Also, we note that since we plot here the two-terminal conductance instead of R_{xx}, the minima occur at different filling factors than those expected for R_{xx} minima ($4m + 2$ for integer m) when $n/n_0 < 4$.

Figure S4.2b is a similar plot for device G1, where the vertical axis is instead the four-terminal resistance R_{xx}. For this sample, a similar phase shift was observed for large filling factors. For relatively small filling factors, the phase shift appears to be within the transition region over the gate voltage range studied.

S5. Horizontal line traces showing the phase shift for sample G2 and G1

In order to further verify the presence of the π phase shift, we show here horizontal gate traces for G2. In Fig. S4.3a, we plot ΔG vs. ν for device G2 with B ranging from 3T to 5T. The phase shift occurs near $n/n_0 = 4$, at a relative filling factor

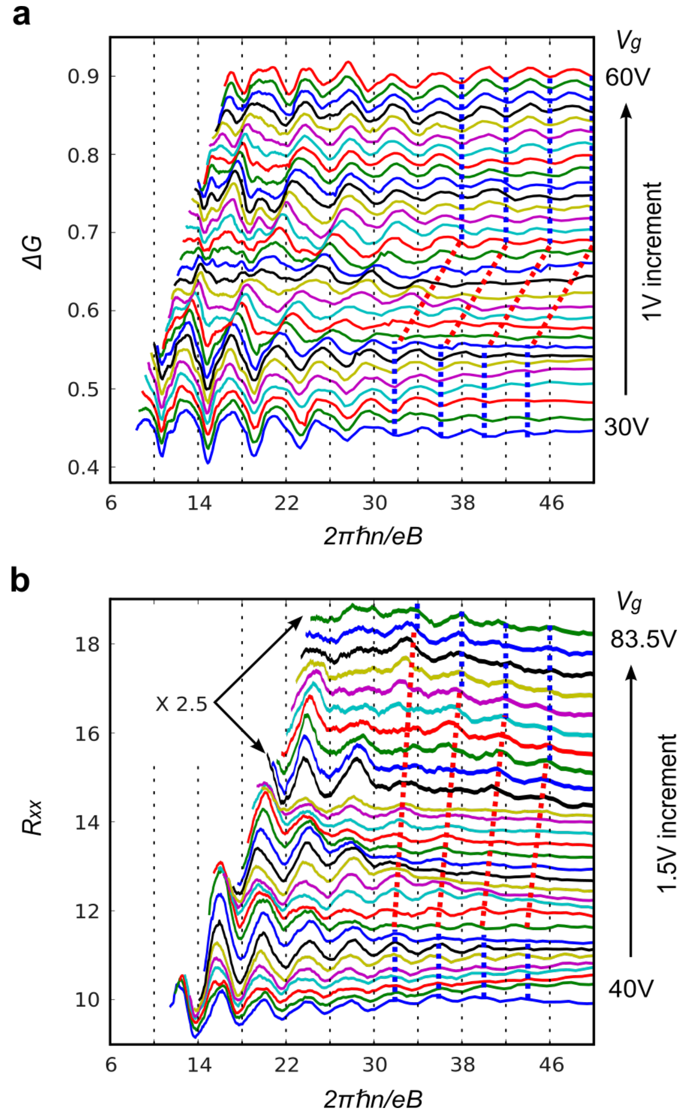

Figure S4.2: **Vertical line traces for sample G2 and G1.** (**a**) Plot of ΔG vs. $\nu = 2\pi n\hbar/eB$, for gate voltages ranging from 30V to 60V (1V increment for each line). Dashed lines are drawn as a guide to the eye. Blue: regions where the phase is stable in gate voltage, following the ΔG minima. Red dashed lines, phase transition region. (**b**) Plot of R_{xx} vs. $\nu = 2\pi n\hbar/eB$, for gate voltage range from 40V to 83.5V (1.5V increment for each line). Dashed lines are drawn as guides to the eye as in (**a**), except following R_{xx} maxima. Vertical scale is expanded by a factor of 2.5 in the region indicated by the arrows to enhance the oscillation visibility.

$\sim$10 from the sDP that occurs just to the right of the Zak oscillation region; for each line trace, the transition point is calculated and drawn as a black circle. To the left of the transition the period of the oscillations is 4 and the maxima in ΔG are aligned with the vertical dashed lines, verifying our capacitance calculations from section S4 are correct. However, near the black circles, the phase starts to shift and a full π shift is observed towards the right end of the traces where instead the minima in ΔG are aligned with the dashed lines. This is shown for example along the red arrow, which connects a maximum to a minimum across the π phase shift. The observed phase shift in the gate traces is insensitive to the zero of charge, since changing this would only uniformly translate the curves.

To perform a similar analysis on sample G1, we plot in Fig. S4.3b the background subtracted ΔR_{xx} vs. ν and expand the vertical scale after the black circles by a factor of 3. A similar π phase shift is observed in the gate traces. To the left of the transition, the vertical dashed lines align with ΔR_{xx} minima, and to the right of the transition they align to the ΔR_{xx} maxima. This is shown by the red arrow, which connects a minimum to a maximum across the transition.

S6. Data from sample G3

We show in Fig. S4.4 additional data from device G3 (R_{xx} vs. B and V_g) that shows secondary Dirac point features. Due to an apparent charge inhomogeneity in the sample, the Landau fan features at different ranges of gate voltage do not extrapolate to the same V_g at $B = 0$, as indicated by in red and black lines in Fig. S4.4. As a result, it is impossible to make a similar analysis for the phase shift as for devices G1 and G2.

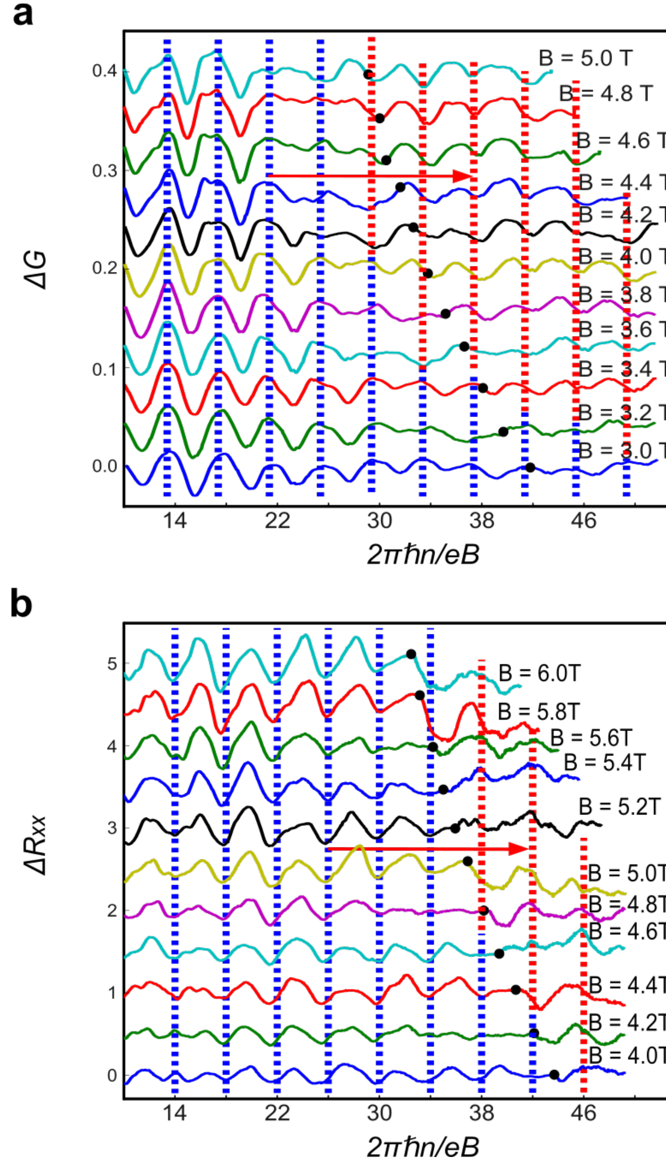

Figure S4.3: **Horizontal line traces for sample G2 and G1.** (**a**) Plot of ΔG vs. $\nu = 2\pi n\hbar/eB$, for B ranging from 3 T to 5 T. Equally spaced dashed lines are drawn as a guide to the eye, where blue follows ΔG maxima and red follows the minima. For each line trace, a black circle (marking a relative filling factor of +10 from sDP) is drawn indicating where the phase shift in the oscillations with respect to $\nu(V_g)$ occurs. (**b**) Plot of ΔR_{xx} vs. $2\pi n\hbar/eB$, for B ranging from 4 T to 6 T. Dashed lines are drawn as guides to the eye as in (**a**), except blue follows ΔR_{xx} minima and red follows ΔR_{xx} maxima. Black circles are as in (**a**). The vertical scale to the right of the black circles is expanded by a factor of 3.

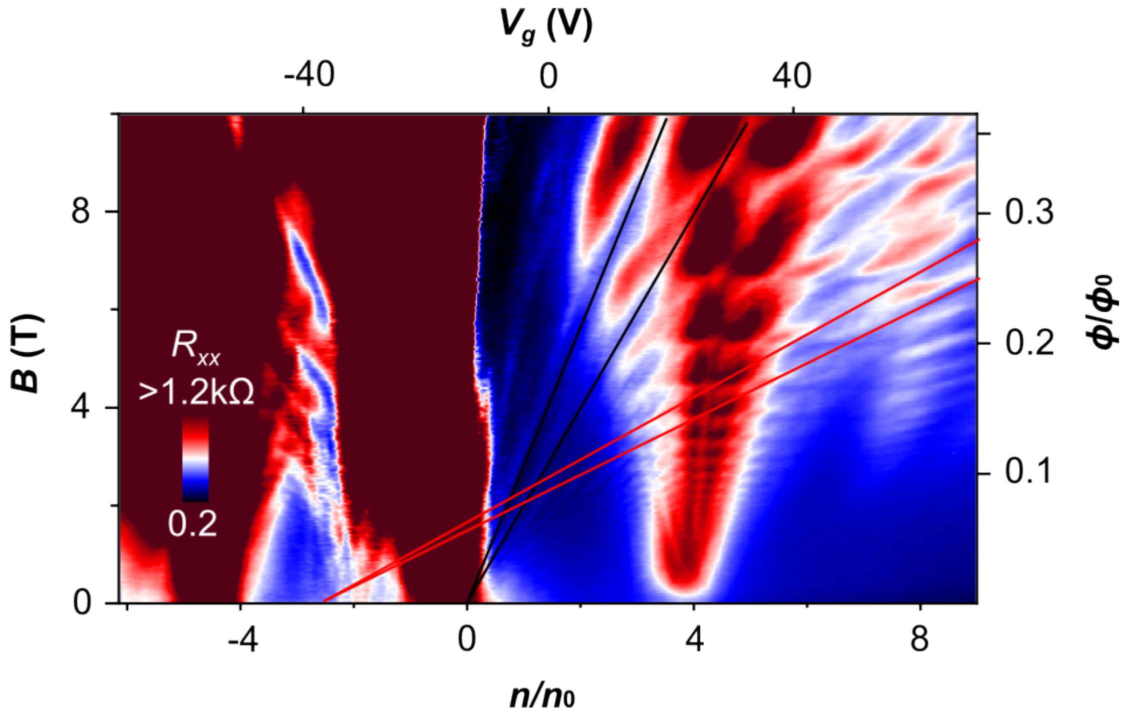

Figure S4.4: **Data for sample G3.** Color plot of R_{xx} vs. gate voltage (top axis)/normalized charge density (bottom axis) and B (left axis)/flux quanta per unit moiré superlattice unit cell (right axis). Red and black lines show extrapolation to zero B of features from $n/n_0 > 4$ (red) and $n/n_0 < 4$ (black).

Chapter 5

Ballistic Transport in Short Graphene cavities

In this chapter, we report our observations on ballistic transport of short graphene cavities encapsulated between two hexagonal boron nitride (hBN) layers. The BN/G/BN sandwich structures[64, 91] allow us to achieve electronic transport with ultra high mobilities (μ) and long mean free path (l). As a consequence, the conductance exhibits quantum interference phenomenon such as Fabry-Pérot oscillations (FPO). When subject to a perpendicular magnetic field (B), we observe a continuous transition from FPO to Shubnikov-de Hass oscillations (SdHO) as B increases. Moreover, near the charge neutrality point, the conductance exhibits small to no dependence on B suggesting signatures of "pseudodiffusive" transport[92].

5.1 Device Fabrication and Characteristics

The BN/G/BN sandwich structures are stacked using a technique that sequencially picks up hBN and graphene layers. Electrical contacts are then made via

one-dimensional carbon chain parallel to the sample edge exposed by inductively coupled plasma (ICP). The details of these techniques are described in detail in chapter 3. To prepare the short BN/G/BN cavities, we first fabricated the device into a Hall bar geometry and tested the device quality. Figure 5.1 shows the low temperature transport characteristics at $T = 1.6$ K. Figure 5.1a plots the resistivity (ρ_{xx}, black) versus charge density (n) at zero B field, and we obtain a field effect mobility $\mu_{FE} \approx 100,000$ cm^2/V·s near the charge neutrality point (CNP) defined by the Drude model $\mu = e^{-1}d\sigma/dn$. The electron mean free path (l) can be extracted using the following relation:

$$\sigma = \frac{2e^2}{h} k_F l, \tag{5.1}$$

where $\sigma = 1/\rho_{xx}$ is the conductivity and $k_F = \sqrt{\pi n}$ is the Fermi wave vector. As we can see, the electron mean free path is above 0.5µm in a wide range of doping levels except very close to the CNP. The above analysis only provides a lower bound estimation of the mean free path as pointed out in Ref.[91] due to boundary scattering when l is approaching the sample width. Figure 5.1b plots ρ_{xx} (black) and Hall conductivity (σ_{xy}, red) near the CNP at $B = 5.5$T. Clearly, Hall plateaus at filling factors of $\nu = \pm 2$ with vanishing ρ_{xx} and $\nu = 0$ with insulating ρ_{xx} ($\sim$ 450kΩ) are well developed; moreover, we also observe the start formation of the $\nu = \pm 1$ quantum Hall plateaus, suggesting the broken symmetry states of the zeroth Landau level in graphene are fully resolved. The observation of $\nu = 0, \pm 1$ quantum Hall states at such low B field further confirms the high quality of our samples.

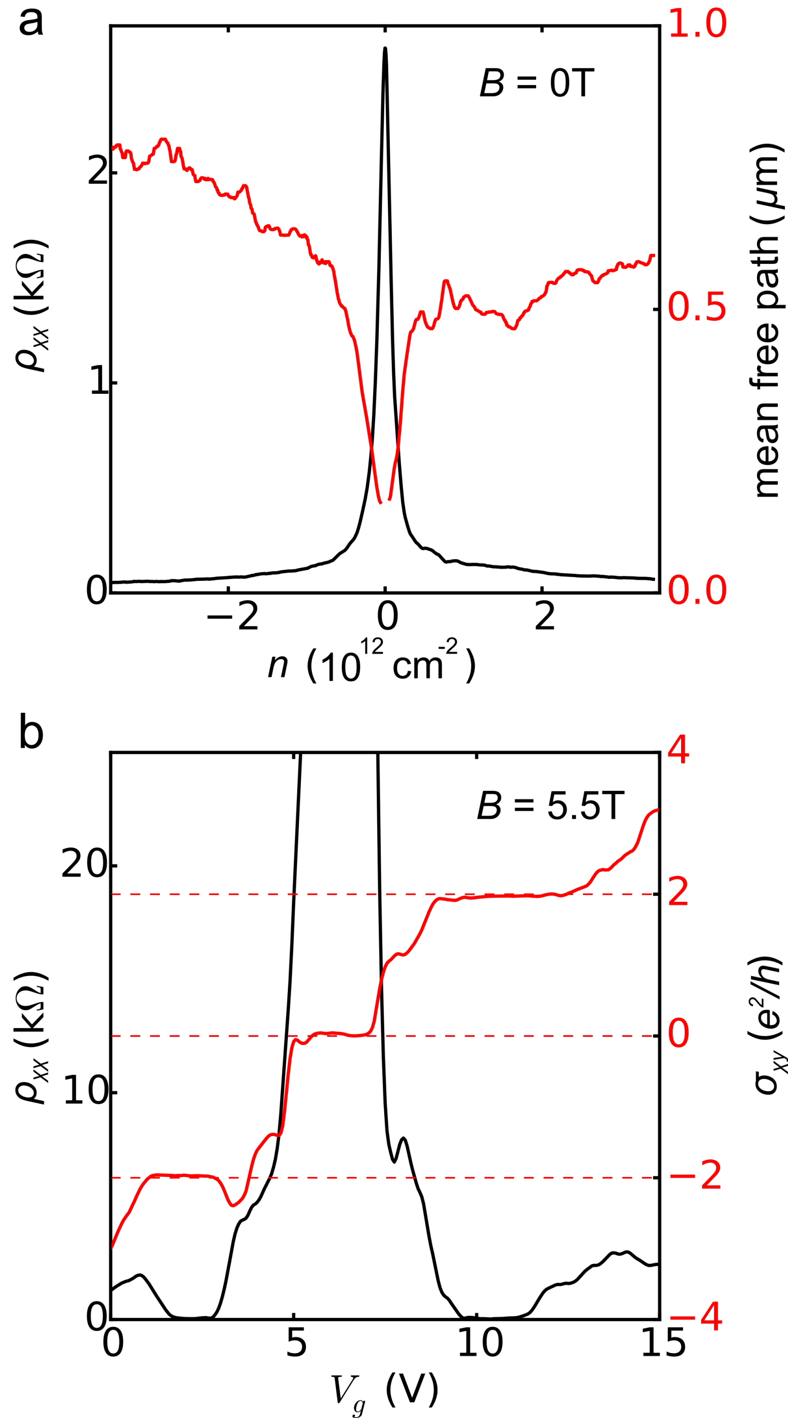

Figure 5.1: Low temperature transport characteristics of BN/G/BN device in Hall bar geometry. (a) Longitudinal resistivity (ρ_{xx}, black) and electron mean free path (l, red) vs. charge density (n) at zero B field. The mean free path near the CNP is not plotted due to a singularity when divided by a zero k_F. (b) ρ_{xx} (black) and Hall conductivity (σ_{xy}, red) vs. gate voltage (V_g). Red dashed lines are for eye guide to the Hall plateaus.

We then perform further lithography and etching steps to cut the Hall bar device into short and wide sections with length of $\sim$ 100nm, $\sim$ 200nm and $\sim$ 300nm. The width of the device is approximately 1μm. A scanning electron microscopy (SEM) image of a finished device is shown in Figure 5.2 with the BN/G/BN cavities outlined by dashed lines.

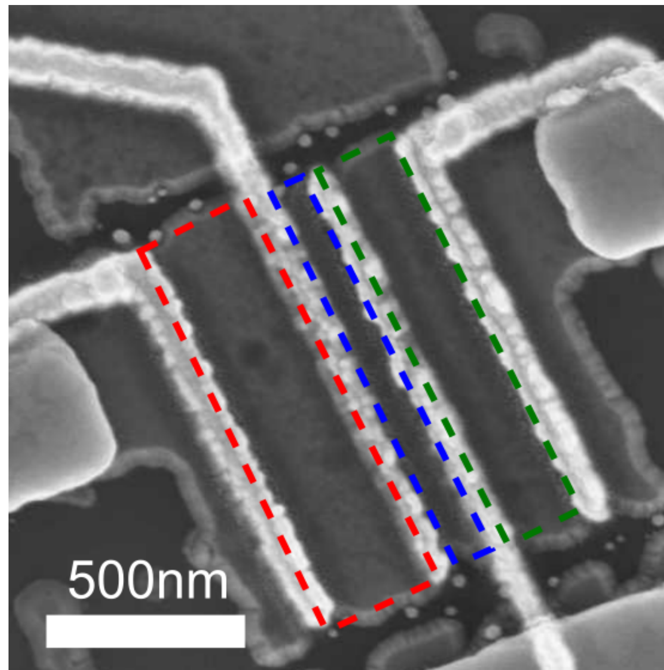

Figure 5.2: Scanning electron microscopy (SEM) image of short-wide BN/G/BN cavities. The red, blue and green dashed lines outline three cavities with length of about 300nm, 100nm and 200nm.

5.2 Fabry-Pérot Oscillations in BN/G/BN Cavities

The length of the devices are shorter than the electron mean free path as plotted in Figure 5.1a. As a consequence, quantum interference effects are expected such as Fabry-Pérot oscillations arising from the ballistic phase coherence transport. As drawn

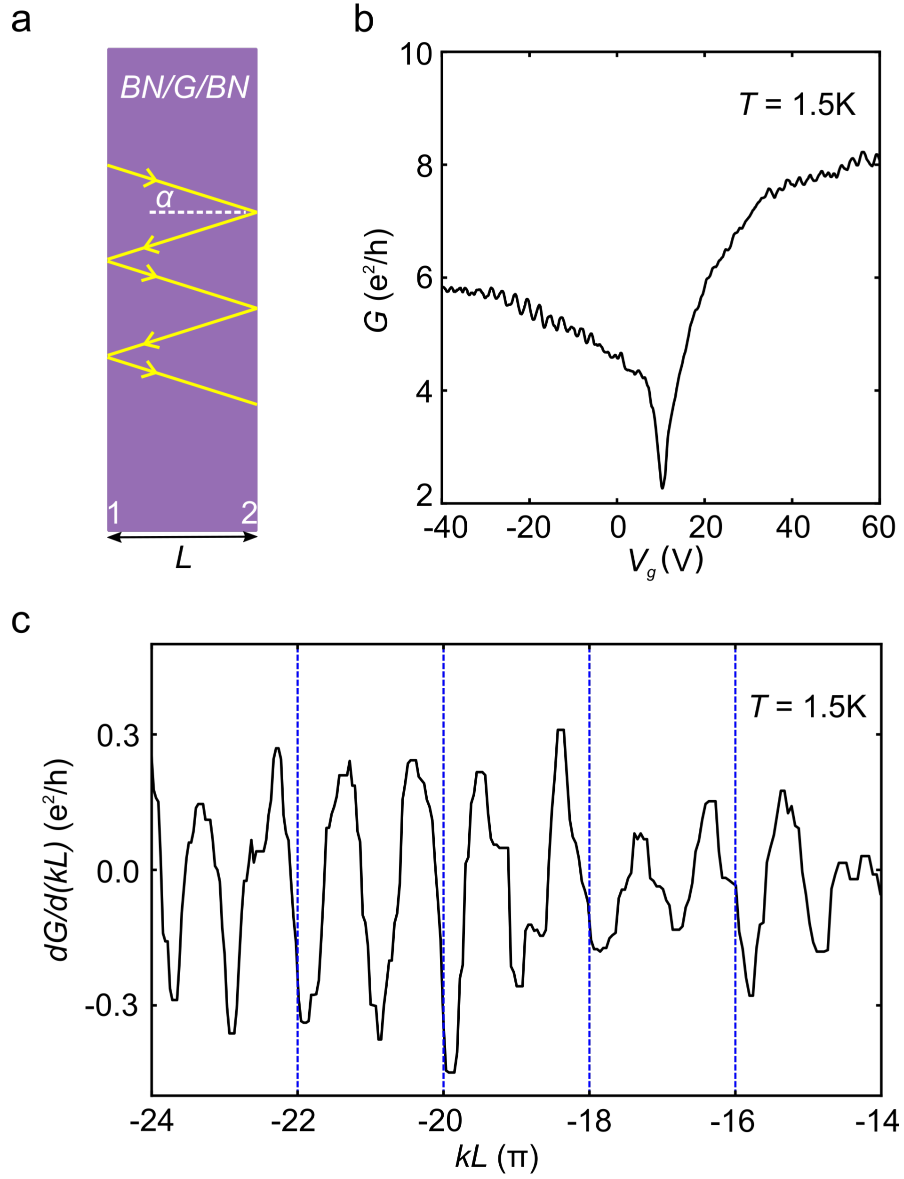

Figure 5.3: Fabry-Pérot oscillations in BN/G/BN cavity. (a) Schematic of the reflection of ballistic electron wave packets on the BN/G/BN boundaries (1 and 2 denotes the two boundaries). Yellow lines: electron trajectories. α corresponds to the incidence angle. (b) Two-terminal conductance (G) vs. gate voltage (V_g). (c) Differentiated conductance ($dG/d(kL)$) vs. kL (in units of π).

in Figure 5.3a is an schematic of the interference effects, where ballistic electrons are reflected off the graphene boundaries. The phase difference between successive reflections

of electron wave packets at zero B field is given by

$$\theta_{WKB} = 2\int_1^2 \boldsymbol{k}\cdot\ d\boldsymbol{r} = 2kL\cos\alpha, \tag{5.2}$$

where $k = \sqrt{\pi n}$ is the Fermi wave vector, L is the sample length and α is the incident angle. Figure 5.3c plots the two-terminal conductance (G) of a 300nm cavity as a function of gate voltage (V_g). We can clearly see G oscillates as k is tuned (by changing V_g). Note that the oscillations are most visible at large carrier doping, consistent with the calculated mean free path trend in Figure 5.1a. Figure 5.3c plots the differentiated conductance ($dG/d(kL)$ vs. kL in the large hole doping region, in which a period of π is observed in agreement with Equation 5.2 at normal incidence ($\alpha = 0°$).

The temperature dependence of the FPO is plotted in Figure 5.4a with the kL range as in Figure 5.3b. The oscillations are persistent up to $\sim$ 16K in this sample. We next try to extract the energy scale (ΔE) of the FPO and the Fermi velocity (V_F) by fitting the oscillations amplitude (standard deviation of dG/dV_g) with the thermal damping model[93]:

$$\delta(dG/dV_g) = A\frac{\xi}{\sinh(\xi)}, \tag{5.3}$$

where $\xi = 2\pi^2 k_B T/\Delta E$ and A is a fitting parameter. This results in $\Delta E \approx 7.59$meV and $v_F \approx 1.10 \times 10^6$ m/s, consistent with previously reported values of graphene on substrates[9, 10, 94].

This effect in graphene has been previously studied in gate defined cavities or suspended samples[15, 93, 95–97]. In our experiments, the cavities are defined by the hard boundaries of the BN/G/BN junctions providing an alternative method to study this type of quantum interference effect. The hard wall boundary conditions also lead to somewhat different behavior as a magnetic field is applied, which will be discussed in the following section.

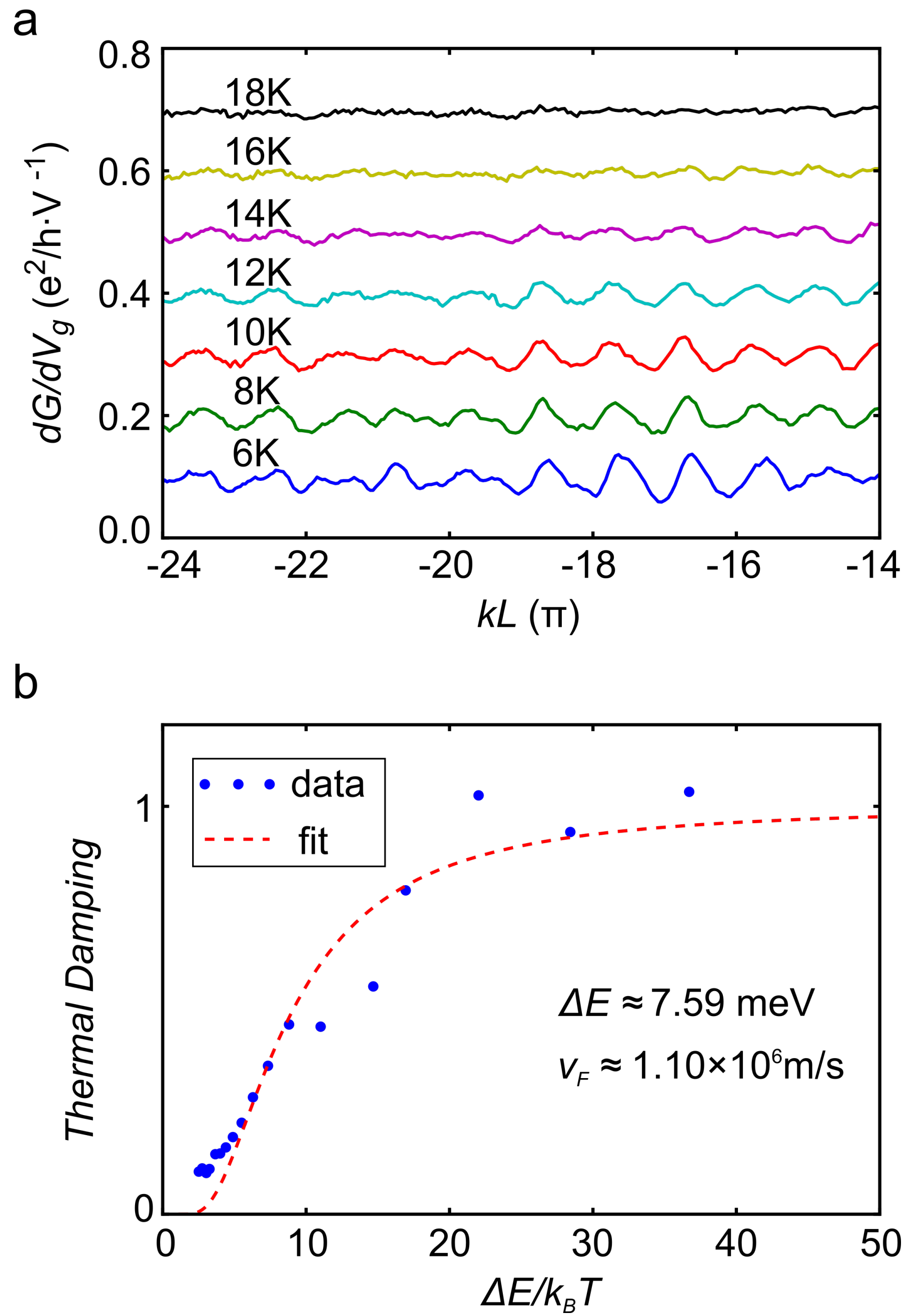

Figure 5.4: (a) Fabry-Pérot oscillations at different temperatures for the same device as in Figure 5.3. The temperature range from 6K to 18K as labeled. (b) Fitting the oscillation amplitude to the thermal damping model. Blue dots represent experimental data while the red line is fitting curve.

5.3 Magnetotransport of BN/G/BN Cavities

In this section, we present magnetotransport data on BN/G/BN cavities. Figure 5.5a plots the background subtracted conductance (ΔG) in gray scale vs. charge density (n) and B for a 300nm cavity. Focusing on the electron side, we can clearly see three different regions of features separated by the red and blue dashed curves. In the high B limit above the blue dashed curve, oscillation features of G in the $B-n$ plane is observed corresponding to Shubnikov-de Hass oscillation (SdHO); in the low B limit below the red dashed curve, G oscillates with n and bends toward high n as B increases; in between the two curves, features in G are mostly smeared out.

The above observations can be explained by considering the relevant length scales in the system, namely the cyclotron radius R_C, the electron mean free path l and sample length L. As illustrated in previous section, the mean free path l of the BN/G/BN cavities is mostly larger than the cavity length L except at the CNP. As a result, the scattering length of the system is determined by L. On the other hand, the cyclotron radius $R_C = k_F l_B^2 = \sqrt{\pi n}\hbar/eB$. Figure 5.5b-e schematically show the different scenarios of R_C compare to L as increasing B, where the yellow curves represent cyclotron orbits. In the low field limit (Figure 5.5b), R_C is larger than L, thus ballistic electrons are reflected off the boundaries and quantum interference effects still hold with an additional phase induced by the curved orbits. As B further increases, when equal or larger than L, cyclotron orbits can no longer reach the other boundary and no reflection takes place. This corresponds to the cases of Figure 5.5c and d. Lastly, when B further increases reaching the limit where $L \geq 2R_C$, electrons can finish at least one complete cyclotron orbit without being scattered (Figure 5.5e) leading to magneto-oscillations known as Shubnikov-de Hass Oscillation as discussed in chapter one.

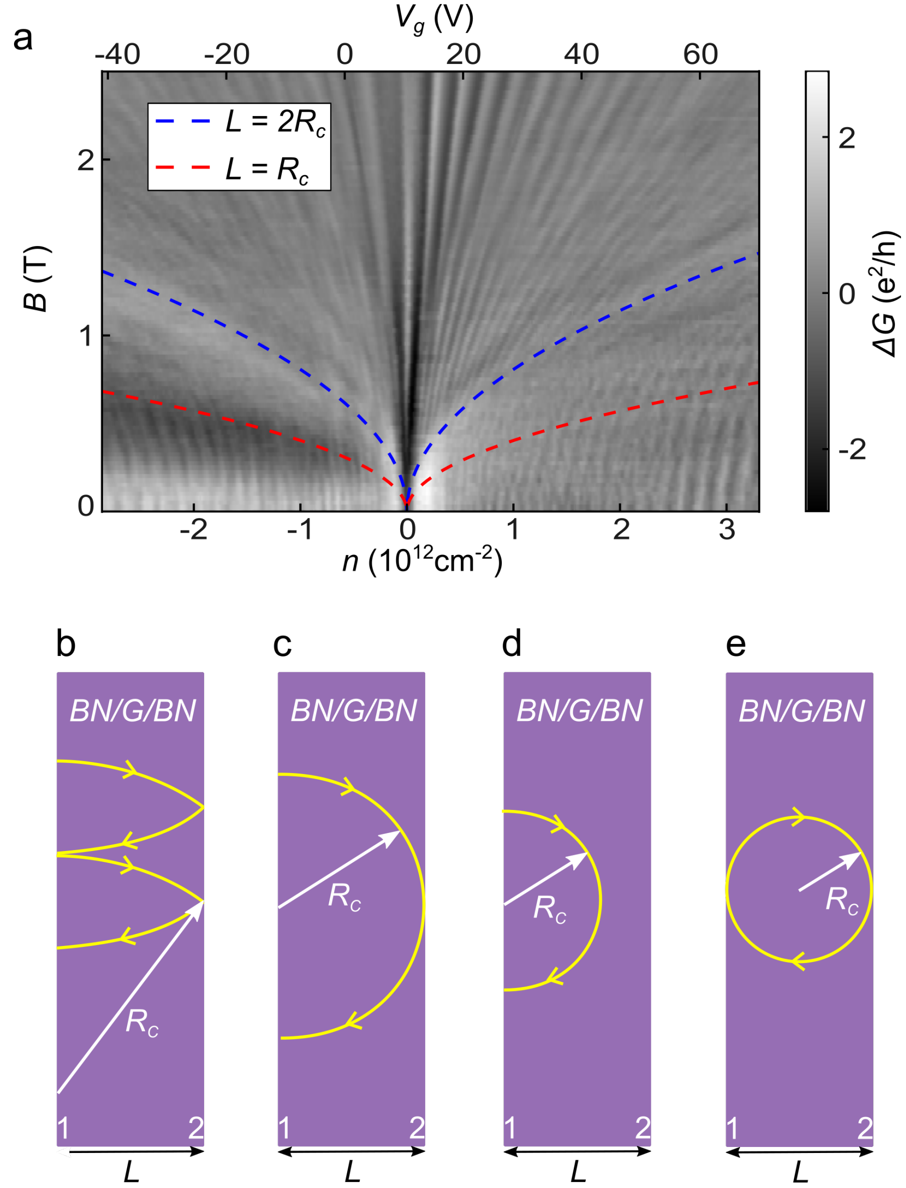

Figure 5.5: Magnetotransport in a 300nm BN/G/BN cavities. (a) Background subtracted conductance (ΔG) vs. V_g (top axis)/n (bottom axis) and B. Blue and red dashed curves correspond to the critical condition when $L = 2R_C$ and $L = 2R_C$ respectively. (b)-(e) cyclotron orbits compare to the sample length L as B increases. The yellow lines represent cyclotron orbits.

Going back to Figure 5.5a, the blue and red dashed curves are indeed related to the critical limits in the above discussion, representing the conditions of $L = 2R_C$ and $L = R_C$ respectively. Quite interestingly, in normal samples where $l \ll L$, the SdHO boundary in B is set by the quality of the sample (l). As a contrast, this boundary in our BN/G/BN cavities is due to finite limit size effect (L).

Similar measurements and analysis are also performed on a 200nm and a 100nm sample, plotted in Figure 5.6a and b. The features in the three regions are again well separated by the $L = 2R_C$ and $L = R_C$ curves but with less clear oscillations than those of the 300nm cavity possibly due to the increased sensitivity to the edge roughness in shorter samples.

Another interesting aspect is the conductivity at the charge neutrality point. Although the density of states in graphene tends to zero when the Fermi level is tuned to Dirac point, the observed conductivity remains finite on the order of e^2/h [1]. For a short and wide graphene strip, the minimum conductivity is predicted to tend to a constant value $4e^2/\pi h$ as the aspect ratio W/L increases in clean graphene[98]. Such deviation from zero conductance results from transport via the evanescent modes near the Dirac point, which is also called "pseudodiffussive" transport[92, 98]. When a magnetic field is applied, Landau quantization leads to SdHO and quantum Hall effects at finite doping. However, at the Dirac point, the cyclotron radius $R_C = k_F l_B^2 = 0$ for any B field and is always smaller than the mean free path (same as sample length L in this case). As a result, the pseudodiffussive transport at the Dirac point is preserved and the conductivity remains constant as B increases[92]. Experimentally, this effect has not be observed possibly because of its extreme sensitivity to finite doping with increasing B.

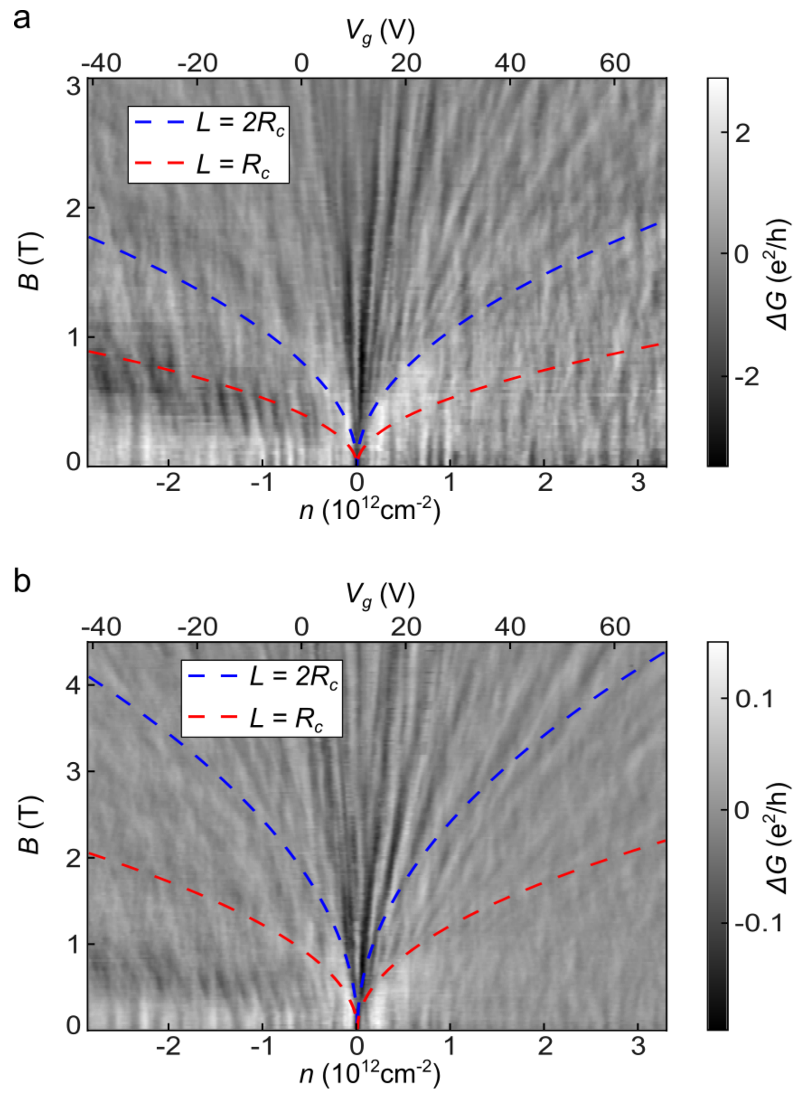

Figure 5.6: Magnetotransport in a 200nm (a) and a 100nm (b) BN/G/BN cavities similar to Figure 5.5a.

In our BN/G/BN cavities, we observed possible signatures of pseudodiffussive transport at charge neutrality point, plotted in Figure 5.7. In Figure 5.7a, the conductivity σ of a 200nm cavity is plotted vs. V_g near the CNP for a magnetic field ranging from 0T to 0.7T with an increment of 0.1T. The observed σ at the CNP remains close to a constant value (which happens to be $4e^2/\pi h$ but different from sample to sample) up to 0.6T. Figure 5.7b plots σ vs. L/l_B for all B measured, again shows the unusual B independent conductivity for L/l_B up to ~ 6. We see similar behavior at the CNP in most of the samples studied.

In summary, we achieved micron-scale mean free path boron nitride encapsulated graphene samples. By fabricating BN/G/BN cavities down to critical lengths smaller than the mean free path, quantum phase coherent effects such as Fabry-Pérot oscillations emerge. Magnetotransport measurements demonstrate transitions from Fabry-Pérot oscillations to Shubnikov-de Hass oscillations by tuning cyclotron radius to critical lengths by changing magnetic field. Magnetotransport data at the Dirac point also shows signatures of pseudodiffussive transport.

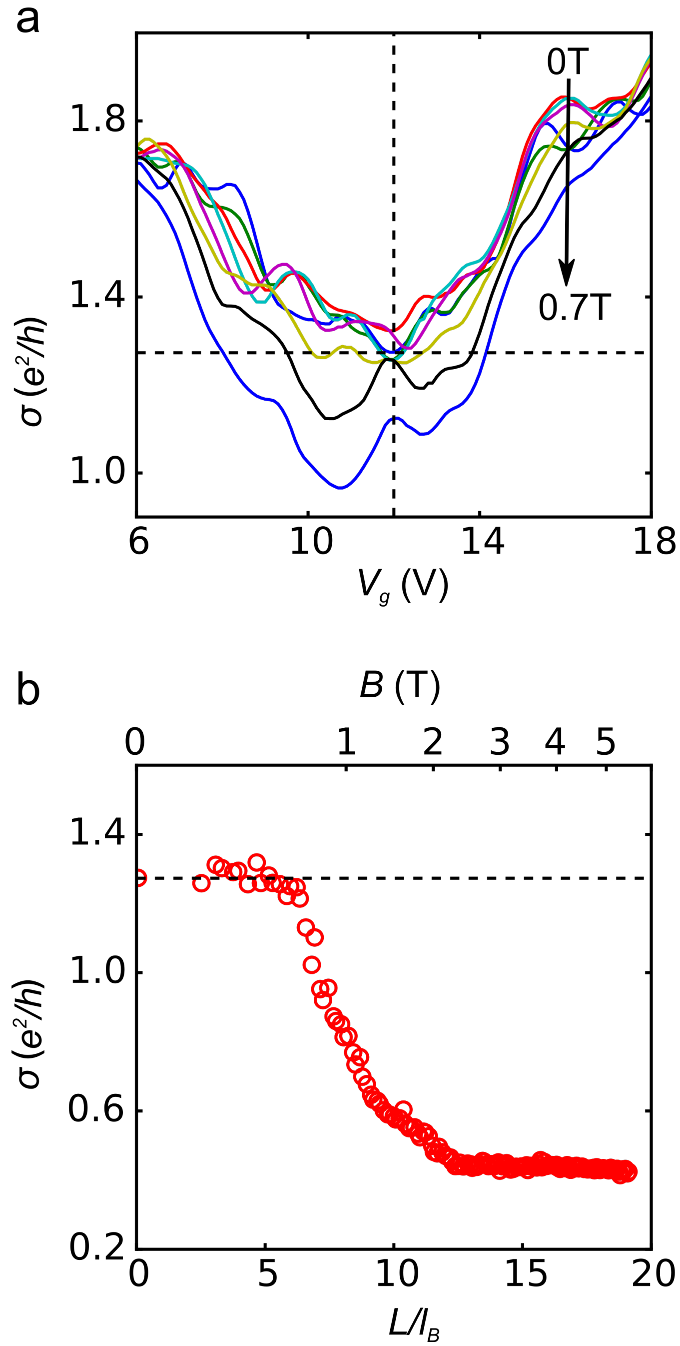

Figure 5.7: (a) Conductivity (σ) vs. V_g near the charge neutrality point (CNP) for B ranging from 0 to 0.7T. The vertical and horizontal dashed lines represent CNP and $\sigma = 4e^2/\pi h$. (b) σ (red circles) vs. L/l_B (bottom axis)/B (top axis) at the Dirac point ($Vg \approx 12V$). The horizontal dashed is the same as in (a).

Chapter 6

Conclusion

In this thesis, we used transport measurements to study the electronic properties of graphene stacked on hexagonal boron nitride in two different scenarios. In the limit of small rotation angle ($<\sim 1^\circ$), the long wavelength moiré superlattice alters graphene's low energy electronic spectrum creating minibands near the superlattice Brillouin zone (sBZ). In magnetic field, commensurate effects lead to a complex self-similar fractal spectrum known as the Hofstadter's butterfly. Our measurements on this system focused on the large electron doping region leads to the observation of a π shift in Berry's phase associated with the change of the topological pseudospin winding number from odd to even when the electron doping level crosses from below to above the minibands Dirac point (s). On the large hole doping region, inversion symmetry breaking induced by the hexagonal boron nitride substrate creates a complex network of polygon pattern with the alternate occurrence of Dirac point features and gap-like features. These observations contribute to the understanding of this highly tunable system, yet more experimental and theoretical works are needed to further explore it.

In the limit of large rotation angle, the high quality of the encapsulated graphene

between two boron nitride crystals allows the intrinsic properties of graphene to be more approachable. By making the sample length shorter than the electronic mean free path, quantum phase coherence transport - Fabry-Pérot oscillations were observed. In the presence of a perpendicular magnetic field, transitions from the Fabry-Pérot type oscillations to Shubnikov-de Hass oscillations was demonstrated and could be explained by comparing the cyclotron radius with the length of the devices. Moreover, conductivity at the charge neutrality point as tuning the magnetic field provides signatures of magneto-pseudodiffussive transport. Further experiments may be done with a corbino disk geometry to investigate the pseudodiffussive behavior for finite doping in resonance with Landau levels[92].

To conclude, the advances in stacking 2D crystals have opened a new route to study material science and the mesoscopic physics associated with it. By combining different 2D materials, there are in principle unlimited possibilities of tailoring the properties of them. For example, stacking graphene with the recent rising material - black phosphorus[99] may induce anisotropic electronic properties in graphene due to the 1D periodic structure of the black phosphorus. Such examples are just too many to list, future work will continue to explore this rich research field.

Bibliography

[1] K. S. Novoselov, A. K. Geim, S. V. Morozov, D. Jiang, Y. Zhang, S. V. Dubonos, I. V. Grigorieva, and A. A. Firsov. Electric field effect in atomically thin carbon films. *Science* 306, pp. 666–669, 2004. DOI: 10.1126/science.1102896.

[2] C. Lee, X. Wei, J. W. Kysar, and J. Hone. Measurement of the elastic properties and intrinsic strength of monolayer graphene. *Science* 321, pp. 385–388, 2008. DOI: 10.1126/science.1157996.

[3] A. A. Balandin, S. Ghosh, W. Bao, I. Calizo, D. Teweldebrhan, F. Miao, and C. N. Lau. Superior thermal conductivity of single-layer graphene. *Nano Letters* 8, pp. 902–907, 2008. DOI: 10.1021/nl0731872.

[4] S. Bae, H. Kim, Y. Lee, X. Xu, J.-S. Park, Y. Zheng, J. Balakrishnan, T. Lei, H. R. Kim, Y. I. Song, Y.-J. Kim, K. S. Kim, B. Özyilmaz, J.-H. Ahn, B. H. Hong, and S. Iijima. Roll-to-roll production of 30-inch graphene films for transparent electrodes. *Nature Nanotech* 5, pp. 574–578, 2010. DOI: 10.1038/nnano.2010.132.

[5] P. R. Wallace. The band theory of graphite. *Phsical Review* 71, pp. 622–634, 1947. DOI: 10.1103/PhysRev.71.622.

[6] C. R. Dean, L. Wang, P. Maher, C. Forsythe, F. Ghahari, Y. Gao, J. Katoch, M. Ishigami, P. Moon, M. Koshino, T. Taniguchi, K. Watanabe, K. L. Shepard,

J. Hone, and P. Kim. Hofstadter's butterfly and the fractal quantum Hall effect in moiré superlattices. *Nature*, pp. 1–5, 2013. DOI: 10.1038/nature12186.

[7] L. A. Ponomarenko, R. V. Gorbachev, G. L. Yu, D. C. Elias, R. Jalil, A. A. Patel, A. Mishchenko, A. S. Mayorov, C. R. Woods, J. R. Wallbank, M. Mucha-Kruczynski, B. A. Piot, M. Potemski, I. V. Grigorieva, K. S. Novoselov, F. Guinea, V. I. Fal'ko, and A. K. Geim. Cloning of Dirac fermions in graphene superlattices. *Nature* 497, pp. 594–597, 2013. DOI: 10.1038/nature12187.

[8] B. Hunt, J. D. Sanchez-Yamagishi, A. F. Young, M. Yankowitz, B. J. LeRoy, K. Watanabe, T. Taniguchi, P. Moon, M. Koshino, P. Jarillo-Herrero, and R. C. Ashoori. Massive Dirac fermions and Hofstadter butterfly in a van der Waals heterostructure. *Science* 340, pp. 1427–1430, 2013. DOI: 10.1126/science.1237240.

[9] K. S. Novoselov, A. K. Geim, S. V. Morozov, D. Jiang, M. I. Katsnelson, I. V. Grigorieva, S. V. Dubonos, and A. A. Firsov. Two-dimensional gas of massless Dirac fermions in graphene. *Nature* 438, pp. 197–200, 2005. DOI: 10.1038/nature04233.

[10] Y. Zhang, Y.-W. Tan, H. L. Stormer, and P. Kim. Experimental observation of the quantum Hall effect and Berry's phase in graphene. *Nature* 438, pp. 201–204, 2005. DOI: 10.1038/nature04235.

[11] A. H. C. Neto, N. M. R. Peres, K. S. Novoselov, and A. K. Geim. The electronic properties of graphene. *Reviews of Modern Physics* 81, pp. 109–162, 2009. DOI: 10.1103/revmodphys.81.109.

[12] M. I. Katsnelson, K. S. Novoselov, and A. K. Geim. Chiral tunnelling and the Klein paradox in graphene. *Nature Physics* 2, pp. 620–625, 2006. DOI: 10.1038/nphys384.

[13] A. Shytov, M. Rudner, and L. Levitov. Klein backscattering and Fabry-Pérot interference in graphene heterojunctions. *Physical Review Letters* 101, p. 156804, 2008. DOI: 10.1103/PhysRevLett.101.156804.

[14] N. Stander, B. Huard, and D. Goldhaber-Gordon. Evidence for Klein tunneling in graphene p-n junctions. *Physics Review Letters* 102, 2009. DOI: 10.1103/physrevlett.102.026807.

[15] A. F. Young and P. Kim. Quantum interference and Klein tunnelling in graphene heterojunctions. *Nature Physics* 5, pp. 222–226, 2009. DOI: 10.1038/nphys1198.

[16] E. McCann and V. I. Fal'ko. Landau-level degeneracy and quantum Hall effect in a graphite bilayer. *Physics Review Letters* 96, p. 086805, 2006. DOI: 10.1103/PhysRevLett.96.086805.

[17] E. H. Hall. On a new action of the magnet on electric currents. *American Journal of Mathematics* 2, pp. 287–92, 1879.

[18] K. v. Klitzing, G. Dorda, and M. Pepper. New method for high-accuracy determination of the fine-structure constant based on quantized Hall resistance. *Physics Review Letters* 45, pp. 494–497, 1980. DOI: 10.1103/PhysRevLett.45.494.

[19] M. O. Goerbig. Quantum Hall effects. 2009.

[20] J. W. McClure. Diamagnetism of graphite. *Physical Review* 104, pp. 666–671, 1956. DOI: 10.1103/physrev.104.666.

[21] M. V. Berry. Quantal phase factors accompanying adiabatic changes. *Proceedings of the Royal Society of London A* 392, pp. 45–57, 1984. DOI: 10.1098/rspa.1984.0023.

[22] D. Xiao, M.-C. Chang, and Q. Niu. Berry phase effects on electronic properties. *Reviews of Modern Physics* 82, pp. 1959–2007, 2010. DOI: 10.1103/revmodphys.82.1959.

[23] J. N. Fuchs, F. Piéchon, M. O. Goerbig, and G. Montambaux. Topological Berry phase and semiclassical quantization of cyclotron orbits for two dimensional electrons in coupled band models. *The European Physical Journal B* 77, pp. 351–362, 2010. DOI: 10.1140/epjb/e2010-00259-2.

[24] C.-H. Park and N. Marzari. Berry phase and pseudospin winding number in bilayer graphene. *Physical Review B* 84, 2011. DOI: 10.1103/physrevb.84.205440.

[25] J. Xue. Berry phase and the unconventional quantum Hall effect in graphene. *arXiv:1309.6714v1*, pp. 1–8, 2013.

[26] K. S. Novoselov, E. McCann, S. V. Morozov, V. I. Fal'ko, M. I. Katsnelson, U. Zeitler, D. Jiang, F. Schedin, and A. K. Geim. Unconventional quantum Hall effect and Berry's phase of 2π in bilayer graphene. *Nature Physics* 2, pp. 177–180, 2006. DOI: 10.1038/nphys245.

[27] H. Min and A. MacDonald. Chiral decomposition in the electronic structure of graphene multilayers. *Physical Review B* 77, p. 155416, 2008. DOI: 10.1103/PhysRevB.77.155416.

[28] S. G. Sharapov, V. P. Gusynin, and H. Beck. Magnetic oscillations in planar systems with the Dirac-like spectrum of quasiparticle excitations. *Physical Review B* 69, p. 075104, 2004. DOI: 10.1103/PhysRevB.69.075104.

[29] I. A. Luk'yanchuk and Y. Kopelevich. Phase analysis of quantum oscillations in graphite. *Physics Review Letters* 93, p. 166402, 2004. DOI: 10.1103/PhysRevLett.93.166402.

[30] P. Blake, E. W. Hill, A. H. Castro Neto, K. S. Novoselov, D. Jiang, R. Yang, T. J. Booth, and A. K. Geim. Making graphene visible. *Applied Physics Letters* 91, p. 063124, 2007. DOI: 10.1063/1.2768624.

[31] K. Bolotin, K. Sikes, Z. Jiang, M. Klima, G. Fudenberg, J. Hone, P. Kim, and H. Stormer. Ultrahigh electron mobility in suspended graphene. *Solid State Communications* 146, pp. 351–355, 2008. DOI: 10.1016/j.ssc.2008.02.024.

[32] X. Du, I. Skachko, A. Barker, and E. Y. Andrei. Approaching ballistic transport in suspended graphene. *Nature Nanotech* 3, pp. 491–495, 2008. DOI: 10.1038/nnano.2008.199.

[33] K. Nomura and A. H. MacDonald. Quantum transport of massless Dirac fermions. *Physics Review Letters* 98, 2007. DOI: 10.1103/physrevlett.98.076602.

[34] E. Hwang, S. Adam, and S. Sarma. Carrier transport in two-dimensional graphene layers. *Physical Review Letters* 98, pp. 2–5, 2007. DOI: 10.1103/PhysRevLett.98.186806.

[35] S. Adam, E. H. Hwang, V. M. Galitski, and S. Das Sarma. A self-consistent theory for graphene transport. *Proceedings of the National Academy of Sciences* 104, pp. 18392–18397, 2007. DOI: 10.1073/pnas.0704772104.

[36] J.-H. Chen, C. Jang, S. Xiao, M. Ishigami, and M. S. Fuhrer. Intrinsic and extrinsic performance limits of graphene devices on SiO2. *Nature Nanotech* 3, pp. 206–209, 2008. DOI: 10.1038/nnano.2008.58.

[37] M. Ishigami, J. H. Chen, W. G. Cullen, M. S. Fuhrer, and E. D. Williams. Atomic structure of graphene on SiO2. *Nano letters* 7, pp. 1643–8, 2007. DOI: 10.1021/nl070613a.

[38] M. I. Katsnelson and a. K. Geim. Electron scattering on microscopic corrugations in graphene. *Philosophical transactions A* 366, pp. 195–204, 2008. DOI: 10.1098/rsta.2007.2157.

[39] S. V. Morozov, K. S. Novoselov, M. I. Katsnelson, F. Schedin, D. C. Elias, J. A. Jaszczak, and A. K. Geim. Giant intrinsic carrier mobilities in graphene and its bilayer. *Physics Review Letters* 100, p. 016602, 2008. DOI: 10.1103/PhysRevLett.100.016602.

[40] S. Fratini and F. Guinea. Substrate-limited electron dynamics in graphene. *Physical Review B* 77, 2008. DOI: 10.1103/physrevb.77.195415.

[41] C. R. Dean, A. F. Young, I. Meric, C. Lee, L. Wang, S. Sorgenfrei, K. Watanabe, T. Taniguchi, P. Kim, K. L. Shepard, and J. Hone. Boron nitride substrates for high-quality graphene electronics. *Nature Nanotech* 5, pp. 722–726, 2010. DOI: 10.1038/nnano.2010.172.

[42] J. Xue, J. Sanchez-Yamagishi, D. Bulmash, P. Jacquod, A. Deshpande, K. Watanabe, T. Taniguchi, P. Jarillo-Herrero, and B. J. LeRoy. Scanning tunnelling microscopy and spectroscopy of ultra-flat graphene on hexagonal boron nitride. *Nat Mater* 10, pp. 282–285, 2011. DOI: 10.1038/nmat2968.

[43] K. Watanabe, T. Taniguchi, and H. Kanda. Direct-bandgap properties and evidence for ultraviolet lasing of hexagonal boron nitride single crystal. *Nature materials* 3, pp. 404–9, 2004. DOI: 10.1038/nmat1134.

[44] M. Yankowitz, J. Xue, D. Cormode, J. D. Sanchez-Yamagishi, K. Watanabe, T. Taniguchi, P. Jarillo-Herrero, P. Jacquod, and B. J. LeRoy. Emergence of superlattice Dirac points in graphene on hexagonal boron nitride. *Nature Physics* 8, pp. 382–386, 2012. DOI: 10.1038/nphys2272.

[45] C. Ortix, L. Yang, and J. van den Brink. Graphene on incommensurate substrates: Trigonal warping and emerging Dirac cone replicas with halved group velocity. *Physical Review B* 86, 2012. DOI: 10.1103/physrevb.86.081405.

[46] M. Kindermann, B. Uchoa, and D. L. Miller. Zero-energy modes and gate-tunable gap in graphene on hexagonal boron nitride. *Physical Review B* 86, p. 115415, 2012. DOI: 10.1103/PhysRevB.86.115415.

[47] J. R. Wallbank, A. A. Patel, M. Mucha-Kruczyński, A. K. Geim, and V. I. Fal'ko. Generic miniband structure of graphene on a hexagonal substrate. *Physical Review B* 87, p. 245408, 2013. DOI: 10.1103/PhysRevB.87.245408.

[48] G. Giovannetti, P. Khomyakov, G. Brocks, P. Kelly, and J. van den Brink. Substrate-induced band gap in graphene on hexagonal boron nitride: AB initio density functional calculations. *Physical Review B* 76, 2007. DOI: 10.1103/physrevb.76.073103.

[49] L. A. Ponomarenko, R. V. Gorbachev, G. L. Yu, D. C. Elias, R. Jalil, A. A. Patel, A. Mishchenko, A. S. Mayorov, C. R. Woods, J. R. Wallbank, M. Mucha-Kruczynski, B. A. Piot, M. Potemski, I. V. Grigorieva, K. S. Novoselov, F. Guinea, V. I. Fal'ko, and A. K. Geim. Cloning of Dirac fermions in graphene superlattices. *Nature* 497, pp. 594–597, 2013. DOI: 10.1038/nature12187.

[50] D. R. Hofstadter. Energy levels and wave functions of Bloch electrons in rational and irrational magnetic fields. *Physical Review B* 14, pp. 2239–2249, 1976. DOI: 10.1103/PhysRevB.14.2239.

[51] R. R. Gerhardts, D. Weiss, and U. Wulf. Magnetoresistance oscillations in a grid potential: Indication of a Hofstadter-type energy spectrum. *Physical Review B* 43, pp. 5192–5195, 1991. DOI: 10.1103/PhysRevB.43.5192.

[52] C. Albrecht, J. Smet, D. Weiss, K. von Klitzing, V. Umansky, and H. Schweizer. Novel magneto-resistance oscillations in short period lateral superlattices. *Physica B* 249-251, pp. 914–917, 1998. DOI: 10.1016/s0921-4526(98)00344-5.

[53] G. H. Wannier. A result not dependent on rationality for Bloch electrons in a magnetic field. *Physica Status Solidi (b)* 88, pp. 757–765, 1978. DOI: 10.1002/pssb.2220880243.

[54] F. H. Claro and G. H. Wannier. Magnetic subband structure of electrons in hexagonal lattices. *Physical Review B* 19, pp. 6068–6074, 1979. DOI: 10.1103/PhysRevB.19.6068.

[55] G. L. Yu, R. V. Gorbachev, J. S. Tu, A. V. Kretinin, Y. Cao, R. Jalil, F. Withers, L. A. Ponomarenko, B. A. Piot, M. Potemski, D. C. Elias, X. Chen, K. Watanabe, T. Taniguchi, I. V. Grigorieva, K. S. Novoselov, V. I. Fal'ko, A. K. Geim, and A. Mishchenko. Erratum: Hierarchy of Hofstadter states and replica quantum Hall ferromagnetism in graphene superlattices. *Nature Physics* 10, pp. 784–784, 2014. DOI: 10.1038/nphys3112.

[56] A. C. Ferrari, J. C. Meyer, V. Scardaci, C. Casiraghi, M. Lazzeri, F. Mauri, S. Piscanec, D. Jiang, K. S. Novoselov, S. Roth, and A. K. Geim. Raman Spectrum

of Graphene and Graphene Layers. *Physics Review Letters* 97, 2006. DOI: 10.1103/physrevlett.97.187401.

[57] A. S. Mayorov, R. V. Gorbachev, S. V. Morozov, L. Britnell, R. Jalil, L. A. Ponomarenko, P. Blake, K. S. Novoselov, K. Watanabe, T. Taniguchi, and A. K. Geim. Micrometer-Scale Ballistic Transport in Encapsulated Graphene at Room Temperature. *Nano Letters* 11, pp. 2396–2399, 2011. DOI: 10.1021/nl200758b.

[58] P. J. Zomer, S. P. Dash, N. Tombros, and B. J. V. Wees. A transfer technique for high mobility graphene devices on commercially available hexagonal boron nitride. *Applied Physics Letters* 232104, pp. 10–12, 2011. DOI: 10.1063/1.3665405.

[59] A. M. Goossens, V. E. Calado, A. Barreiro, K. Watanabe, T. Taniguchi, and L. M. K. Vandersypen. Mechanical cleaning of graphene. *Applied Physics Letters* 100, p. 073110, 2012. DOI: 10.1063/1.3685504.

[60] L. A. Ponomarenko, A. K. Geim, A. A. Zhukov, R. Jalil, S. V. Morozov, K. S. Novoselov, I. V. Grigorieva, E. H. Hill, V. V. Cheianov, V. I. Fal'ko, K. Watanabe, T. Taniguchi, and R. V. Gorbachev. Tunable metal–insulator transition in double-layer graphene heterostructures. *Nature Physics* 7, pp. 958–961, 2011. DOI: 10.1038/nphys2114.

[61] T. Taychatanapat, K. Watanabe, T. Taniguchi, and P. Jarillo-herrero. Quantum Hall effect and Landau-level crossing of Dirac fermions in trilayer graphene. *Nature Physics* 7, pp. 1–5, 2011. DOI: 10.1038/nphys2008.

[62] Y.-C. Lin, C.-C. Lu, C.-H. Yeh, C. Jin, K. Suenaga, and P.-W. Chiu. Graphene annealing: how clean can it be? *Nano Letters* 12 22149394, pp. 414–419, 2012. DOI: 10.1021/nl203733r.

[63] Z. Cheng, Q. Zhou, C. Wang, Q. Li, C. Wang, and Y. Fang. Toward Intrinsic Graphene Surfaces: A Systematic Study on Thermal Annealing and Wet-Chemical Treatment of SiO2-Supported Graphene Devices. *Nano Letters* 11 21218829, pp. 767–771, 2011. DOI: 10.1021/nl103977d.

[64] L. Wang, I. Meric, P. Y. Huang, Q. Gao, Y. Gao, H. Tran, T. Taniguchi, K. Watanabe, L. M. Campos, D. A. Muller, J. Guo, P. Kim, J. Hone, K. L. Shepard, and C. R. Dean. One-dimensional electrical contact to a two-dimensional material. *Science* 342, pp. 614–617, 2013. DOI: 10.1126/science.1244358.

[65] M. A. Meitl, Z.-T. Zhu, V. Kumar, K. J. Lee, X. Feng, Y. Y. Huang, I. Adesida, R. G. Nuzzo, and J. A. Rogers. Transfer printing by kinetic control of adhesion to an elastomeric stamp. *Nature Materials* 5, pp. 33–38, 2005. DOI: 10.1038/nmat1532.

[66] A. Castellanos-Gomez, M. Buscema, R. Molenaar, V. Singh, L. Janssen, H. S. J. van der Zant, and G. A. Steele. Deterministic transfer of two-dimensional materials by all-dry viscoelastic stamping. *2D Materials* 1, p. 011002, 2014. DOI: 10.1088/2053-1583/1/1/011002.

[67] Q. Yu, J. Lian, S. Siriponglert, H. Li, Y. P. Chen, and S.-S. Pei. Graphene segregated on Ni surfaces and transferred to insulators. *Applied Physics Letters* 93, p. 113103, 2008. DOI: 10.1063/1.2982585.

[68] X. Li, W. Cai, J. An, S. Kim, J. Nah, D. Yang, R. Piner, A. Velamakanni, I. Jung, E. Tutuc, S. K. Banerjee, L. Colombo, and R. S. Ruoff. Large-area synthesis of high-quality and uniform graphene films on copper foils. *Science* 324, pp. 1312–1314, 2009. DOI: 10.1126/science.1171245.

[69] K. S. Kim, Y. Zhao, H. Jang, S. Y. Lee, J. M. Kim, K. S. Kim, J.-H. Ahn, P. Kim, J.-Y. Choi, and B. H. Hong. Large-scale pattern growth of graphene films for stretchable transparent electrodes. *Nature* 457, pp. 706–10, 2009. DOI: 10.1038/nature07719.

[70] R. Sachs, Z. Lin, P. Odenthal, R. Kawakami, and J. Shi. Direct comparison of graphene devices before and after transfer to different substrates. *Applied Physics Letters* 104, p. 033103, 2014. DOI: 10.1063/1.4862063.

[71] C. R. Woods, L. Britnell, A. Eckmann, R. S. Ma, J. C. Lu, H. M. Guo, X. Lin, G. L. Yu, Y. Cao, R. V. Gorbachev, A. V. Kretinin, J. Park, L. A. Ponomarenko, M. I. Katsnelson, Y. N. Gornostyrev, K. Watanabe, T. Taniguchi, C. Casiraghi, H.-j. Gao, A. K. Geim, and K. S. Novoselov. Commensurate–incommensurate transition in graphene on hexagonal boron nitride. *Nature Physics* 10, pp. 451–456, 2014. DOI: 10.1038/NPHYS2954.

[72] J. C. W. Song, P. Samutpraphoot, and L. S. Levitov. Topological bands in G/h-BN heterostructures. *arXiv:1404.4019v1*, pp. 1–6.

[73] X. Chen, J. R. Wallbank, A. A. Patel, M. Mucha-Kruczyński, E. McCann, and V. I. Fal'ko. Dirac edges of fractal magnetic minibands in graphene with hexagonal moiré superlattices. *Physical Review B* 89, 2014. DOI: 10.1103/physrevb.89.075401.

[74] C.-H. Park, L. Yang, Y.-W. Son, M. Cohen, and S. Louie. New generation of massless dirac fermions in graphene under external periodic potentials. *Physical Review Letters* 101, pp. 1–4, 2008. DOI: 10.1103/PhysRevLett.101.126804.

[75] F. Guinea and T. Low. Band structure and gaps of triangular graphene superlattices. *Philosophical transactions. Series A, Mathematical, physical, and engineering sciences* 368, pp. 5391–402, 2010. DOI: 10.1098/rsta.2010.0214.

[76] D. Weiss, K. von Klitzing, K. Ploog, and G. Weimann. Landau level broadening and Van Hove singularities in lateral surface superlattices. *Surface Science* 229, pp. 88–91, 1990. DOI: 10.1016/0039-6028(90)90841-u.

[77] T. Schlösser, K. Ensslin, J. P. Kotthaus, and M. Holland. Landau subbands generated by a lateral electrostatic superlattice - chasing the Hofstadter butterfly. *Semiconductor Science Technology* 11, pp. 1582–1585, 1996. DOI: 10.1088/0268-1242/11/11s/022.

[78] Y. Nakamura, T. Inoshita, and H. Sakaki. Novel magneto-resistance oscillations in laterally modulated two-dimensional electrons with 20nm periodicity formed on vicinal GaAs (111)B substrates. *Physica E* 2, pp. 944–948, 1998. DOI: 10.1016/s1386-9477(98)00193-3.

[79] M. Geisler, J. Smet, V. Umansky, K. von Klitzing, B. Naundorf, R. Ketzmerick, and H. Schweizer. Detection of a Landau Band-Coupling-Induced Rearrangement of the Hofstadter Butterfly. *Physics Review Letters* 92, 2004. DOI: 10.1103/physrevlett.92.256801.

[80] C. Albrecht, J. Smet, D. Weiss, K. von Klitzing, V. Umansky, and H. Schweizer. Novel magneto-resistance oscillations in short period lateral superlattices. *Physica B: Condensed Matter* 249-251, pp. 914–917, 1998. DOI: 10.1016/s0921-4526(98)00344-5.

[81] F. H. Claro and G. H. Wannier. Magnetic subband structure of electrons in hexagonal lattices. *Physical Review B* 19, pp. 6068–6074, 1979. DOI: 10.1103/PhysRevB.19.6068.

[82] P. Streda. Quantised Hall effect in a two-dimensional periodic potential. *Journal of Physics C: Solid State Physics* 15, pp. L1299–L1303, 1982. DOI: 10.1088/0022-3719/15/36/006.

[83] A. H. MacDonald. Landau-level subband structure of electrons on a square lattice. *Physical Review B* 28, pp. 6713–6717, 1983. DOI: 10.1103/PhysRevB.28.6713.

[84] R. de Gail, M. O. Goerbig, and G. Montambaux. Magnetic spectrum of trigonally warped bilayer graphene: semiclassical analysis, zero modes, and topological winding numbers. *Physical Review B* 86, p. 045407, 2012. DOI: 10.1103/PhysRevB.86.045407.

[85] E. D. Haidemenakis, ed. *Physics of solids in intense magnetic fields.* Springer Science Business Media, 1969. DOI: 10.1007/978-1-4899-5508-1.

[86] A. S. Mayorov, D. C. Elias, M. Mucha-Kruczynski, R. V. Gorbachev, T. Tudorovskiy, A. Zhukov, S. V. Morozov, M. I. Katsnelson, V. I. Fal'ko, A. K. Geim, and K. S. Novoselov. Interaction-driven spectrum reconstruction in bilayer Graphene. *Science* 333, pp. 860–863, 2011. DOI: 10.1126/science.1208683.

[87] J. Zak. Magnetic translation group. II. Irreducible representations. *Phsical Review* 134, pp. 1607–1611, 1964. DOI: 10.1103/PhysRev.134.A1607.

[88] M.-C. Chang and Q. Niu. Berry phase, hyperorbits, and the Hofstadter spectrum. *Physics Review Letters* 75, pp. 1348–1351, 1995. DOI: 10.1103/PhysRevLett.75.1348.

[89] V. S. Tsoi, J. Bass, and P. Wyder. Studying conduction-electron/interface interactions using transverse electron focusing. *Reviews of Modern Physics* 71, pp. 1641–1693, 1999. DOI: 10.1103/RevModPhys.71.1641.

[90] T. Taychatanapat, K. Watanabe, T. Taniguchi, and P. Jarillo-Herrero. Electrically tunable transverse magnetic focusing in graphene. *Nature Physics* 9, pp. 225–229, 2013. DOI: 10.1038/nphys2549.

[91] A. S. Mayorov, R. V. Gorbachev, S. V. Morozov, L. Britnell, R. Jalil, L. A. Ponomarenko, P. Blake, K. S. Novoselov, K. Watanabe, T. Taniguchi, and A. K. Geim. Micrometer-scale ballistic transport in encapsulated graphene at room temperature. *Nano Letters* 11 21574627, pp. 2396–2399, 2011. DOI: 10.1021/nl200758b.

[92] E. Prada, P. San-Jose, B. Wunsch, and F. Guinea. Pseudodiffusive magnetotransport in graphene. *Physical Review B* 75, p. 113407, 2007. DOI: 10.1103/PhysRevB.75.113407.

[93] A. Varlet, M.-H. Liu, V. Krueckl, D. Bischoff, K. Watanabe, T. Taniguchi, K. Richter, K. Ensslin, and T. Ihn. Fabry-Pérot interference in gapped bilayer graphene with broken anti-Klein tunneling. *Physics Review Letter* 113, p. 116601, 2014. DOI: 10.1103/PhysRevLett.113.116601.

[94] J. Xue, J. Sanchez-Yamagishi, D. Bulmash, P. Jacquod, A. Deshpande, K. Watanabe, T. Taniguchi, P. Jarillo-Herrero, and B. J. LeRoy. Scanning tunnelling microscopy and spectroscopy of ultra-flat graphene on hexagonal boron nitride. *Nature materials* 10, pp. 282–5, 2011. DOI: 10.1038/nmat2968.

[95] L. C. Campos, a. F. Young, K. Surakitbovorn, K. Watanabe, T. Taniguchi, and P. Jarillo-Herrero. Quantum and classical confinement of resonant states in a trilayer

graphene Fabry-Pérot interferometer. *Nature communications* 3, p. 1239, 2012. DOI: 10.1038/ncomms2243.

[96] P. Rickhaus, R. Maurand, M.-H. Liu, M. Weiss, K. Richter, and C. Schönenberger. Ballistic interferences in suspended graphene. *Nature communications* 4, p. 2342, 2013. DOI: 10.1038/ncomms3342.

[97] M. Oksanen, A. Uppstu, A. Laitinen, D. J. Cox, M. F. Craciun, S. Russo, A. Harju, and P. Hakonen. Single-mode and multimode Fabry-Pérot interference in suspended graphene. *Physical Review B* 89, 2014. DOI: 10.1103/physrevb.89.121414.

[98] J. Tworzydło, B. Trauzettel, M. Titov, A. Rycerz, and C. Beenakker. Sub-poissonian shot noise in graphene. *Physics Review Letters* 96, 2006. DOI: 10.1103/physrevlett.96.246802.

[99] L. Li, Y. Yu, G. J. Ye, Q. Ge, X. Ou, H. Wu, D. Feng, X. H. Chen, and Y. Zhang. Black phosphorus field-effect transistors. *Nature Nanotech* 9, pp. 372–377, 2014. DOI: 10.1038/nnano.2014.35.